J Mater Sci (2026) 61:23812–23834

Electronic materials

Phase-pure $MAPbBr_3$ thin films prepared by room-temperature powder aerosol deposition (PAD) and their optical and electrical properties

Tianshan Xu[1,*], Markus Griesbach[2], Till Scholz[1], Daniel Paulus[1], Martin Hämmerle[1], Anna Köhler[2], and Ralf Moos[1,*]

[1] Department of Functional Materials, University of Bayreuth, 95440 Bayreuth, Germany
[2] Soft Matter Optoelectronics, Department of Physics, and Bayreuth Institute of Macromolecular Research (BIMF), and Bavarian Polymer Institute (BPS), University of Bayreuth, 95440 Bayreuth, Germany

Received: 23 March 2026
Accepted: 4 June 2026
Published online: 1 July 2026

ABSTRACT

Preparing $MAPbBr_3$ films with thicknesses beyond a few micrometers remains challenging because solution-based deposition—particularly when multiple coating steps are required—can induce solvent-related film cracking and defects, while thermal exposure can accelerate degradation and compromise phase integrity. Here, we demonstrate that room-temperature powder aerosol deposition (PAD) enables the fabrication of dense, mechanically consolidated methylammonium lead bromide ($MAPbBr_3$) films with thicknesses ranging from several micrometers up to several tens of micrometers. The high-velocity particle impact inherent to PAD does not compromise phase purity or crystal structure; instead, the deposited particles fracture into nanocrystallites (~ 90 nm) exhibiting low microstrain. Optical characterization confirms that the bandgap (~ 2.3 eV) remains unchanged relative to the precursor powder, demonstrating that the electronic structure remains largely preserved during the aerosol deposition process. Temperature-dependent impedance spectroscopy (293–383 K) reveals thermally activated ionic transport with activation energies of 0.55–0.59 eV, consistent with bromide vacancy formation and migration. Analysis of the dielectric loss tangent within the Trukhan framework gives an ionic diffusion coefficient of 3.1×10^{-8} cm^2 s^{-1}, an ionic mobility of 1.2×10^{-6} cm^2 V^{-1} s^{-1}, and a mobile ion concentration of 2.6×10^{16} cm^{-3} at 293 K. This study establishes the first systematic investigation of ionic transport in PAD halide perovskite films, providing insight into bulk ion migration and the associated electrode interfacial polarization.

Handling Editor: Kevin Jones.

Address correspondence to E-mail: functional.materials@uni-bayreuth.des; functional.materials@uni-bayreuth.de

https://doi.org/10.1007/s10853-026-13159-z

Introduction

Halide perovskites have emerged as a highly promising class of semiconducting materials due to their outstanding optoelectronic properties, including strong optical absorption, long charge-carrier diffusion lengths, and defect tolerance [1–3]. Among halide perovskites, $MAPbBr_3$ ($MA = CH_3NH_3^+$) has attracted considerable attention owing to its relatively wide bandgap (~ 2.3 eV), making it particularly suitable for green light-emitting diodes [4], photodetectors [5], and solar cells [6, 7]. Furthermore, bromide-based perovskites exhibit enhanced structural and phase stability compared to iodide perovskites. This is attributed to the stronger Pb–Br bonding, making $MAPbBr_3$ a promising candidate for stable optoelectronic devices [8].

Despite the favorable intrinsic optoelectronic properties of halide perovskites, their effective utilization in devices critically depends on precise control over thin-film formation [9, 10]. Over the past years, a wide range of deposition techniques have been investigated for the fabrication of perovskite layers, most of which rely on solution-based processing routes such as spin coating [11], blade coating [12], slot-die coating [13] or inkjet printing [14]. In these approaches, perovskite film formation typically occurs from precursor solutions, often relying on harmful and environmentally problematic solvents such as dimethylformamide (DMF) or dimethylsulfoxide (DMSO) [15].

One solvent-free processing route is opened by the powder aerosol deposition (PAD) technique, which enables the deposition of dense, solid layers from dry, aerosolized powders onto a wide range of substrates at room temperature. In the PAD process, powder particles are dispersed in a carrier gas and accelerated by a pressure difference through a nozzle toward a substrate, where their high kinetic energy leads to impact-driven consolidation and the formation of dense films [16]. For halide perovskite applications, PAD enables the separation of material synthesis and film formation while offering a scalable route to fabricate layers with thicknesses from less than 1 µm [17] up to several hundred µm [18, 19]. In 2016, Panzer et al. [20] successfully used PAD to deposit $CH_3NH_3PbI_3$ films, proving the viability of the technique for the processing of lead halide perovskites. Subsequently, Biberger et al. [21] reported the first fully functional solar cells incorporating aerosol-deposited perovskite absorber layers. PAD has also been used to fabricate all-inorganic cesium lead halide perovskites such as $CsPbBr_3$, further highlighting the broader research interest in PAD-based processing of halide perovskites [22, 23].

However, PAD remains strongly material-dependent. For example, different halide perovskites can exhibit distinct powder characteristics after ball milling, such as particle size, morphology and agglomeration state, which could influence aerosol transport, particle fracture behavior and the resulting film quality. Therefore, the PAD process parameters optimized for one perovskite composition cannot be directly transferred to another. Consequently, the deposition of $MAPbBr_3$ has proven to be challenging, and aerosol-deposited $MAPbBr_3$ films have not been demonstrated so far. Here, we identify the reasons for this and demonstrate the fabrication of films with thicknesses from approximately 2 to 50 µm by adjusting the number of scans.

The resulting $MAPbBr_3$ films were further characterized in terms of their structural, optical, and electrical properties. SEM and XRD were used to assess the phase purity and microstructure of both the starting powders and the aerosol-deposited films. The optical properties of $MAPbBr_3$ powders and aerosol-deposited films were examined by steady-state and time-resolved photoluminescence spectroscopy. The electrical response of the aerosol-deposited $MAPbBr_3$ films was analyzed using temperature-dependent impedance spectroscopy to elucidate thermally activated ionic transport processes. The distinct relaxation features observed in the impedance spectra enabled us to quantitatively extract ionic transport parameters, including the activation energy, diffusion coefficient, ionic mobility and mobile ion concentration. This study presents the first systematic investigation of ionic transport in mechanically consolidated hybrid halide perovskite films prepared by PAD. The extracted activation energies are consistent with reported values for bromide vacancy migration, indicating that halide defects play a dominant role in ionic transport within these nanocrystalline films.

Experimental section

Powder synthesis

To synthesize $MAPbBr_3$ powders, 1.344 g methylammonium bromide (MABr, Greatcell Solar Materials) and 4.404 g lead bromide ($PbBr_2$, Sigma-Aldrich) were weighed under ambient conditions into zirconia milling jars containing 25 zirconia milling balls (10 mm diameter). 8 ml of cyclohexane was added as a milling agent. The mixture was processed in a Fritsch "Pulverisette 5/4 " planetary mill operated at 400 rpm. The total milling time was 50 min, with 5 min milling intervals followed by 20 min cooling breaks to prevent excessive heating of the milling jar. After milling, the cyclohexane was left to evaporate under ambient conditions for approximately 20 min. The dried powder was subsequently sieved through a 63 μm mesh.

Film deposition

Substrates and geometry

ITO-coated glass substrates with SnO_2 coating were used as substrates for depositing the $MAPbBr_3$ films for subsequent structural characterization. The substrates were cleaned in an ultrasonic bath using a detergent solution (Hellmanex), deionized water, and isopropanol, followed by UV–ozone treatment. SnO_2 nanoparticles (Alfa Aesar 15wt% in H_2O) were spin-coated onto the cleaned substrates at 3000 rpm for 30 s, and the substrates were annealed at 160 °C for 30 min and subsequently treated with UV–ozone again before deposition.

For electrical characterization, alumina substrates (96% purity) patterned with screen-printed carbon interdigitated electrodes (C-IDEs) were used. The IDEs were fabricated by screen printing DuPont 7102 carbon paste, followed by a thermal treatment step at 250 °C for 10 h to ensure sufficient consolidation and electrical conductivity of the carbon electrode structure. The electrode design comprises 29 fingers, each 4 mm in length, 110 μm in width, and separated by a 100 μm gap. A schematic of the IDE geometry is shown in SI Fig. S22.

Powder aerosol deposition method

The films were fabricated using a custom-made PAD apparatus. The setup in our laboratory and its fundamentals can be found in our previous publications [19, 21]. The $MAPbBr_3$ films were produced via PAD, as schematically illustrated in Fig. 1. In the PAD process, micrometer-sized $MAPbBr_3$ powder particles are dispersed in nitrogen within an aerosol generation chamber, forming an aerosol that is transported into a deposition chamber operated under reduced pressure. Driven by the pressure difference between the aerosol generation chamber and the low-pressure deposition chamber, the aerosolized powder is accelerated toward the deposition chamber through a converging slit nozzle. The resulting high particle velocities prior to impact on the substrate lead to room-temperature impact consolidation (RTIC) [18].

To enable deposition under low aerosol mass flow conditions and promote the breakup of weak agglomerates, thereby achieving uniform $MAPbBr_3$ thin films, a combination of an ejector–separator unit and an inertial separator with a collecting tube, following the design reported by Biberger et al. [21], was employed. A detailed description of the ejector–separator unit and an inertial separator is provided in Sect. "From powder to film". The deposition parameters used in this study are listed in Table 1.

Characterization methods

X-ray diffraction

X-ray diffraction (XRD) measurements of powder samples and selected films were taken at beamline P02.1 of PETRA III at the German Electron Synchrotron (DESY), Hamburg, Germany [24]. The measurement was taken in a Debye–Scherrer-like setup. A wavelength of 0.20738 Å was used, which corresponds to a photon energy of approximately 60 keV. A Varex XRD 4343CT detector (150 × 150 μm^2 pixel size, 2880 × 2880 pixel area) was placed 2 m behind the sample holder. The powder and film samples were mounted on Kapton foil using Kapton tape and fixed in a high-throughput sample holder. During the beamtime, a Si NIST 640 g standard reference material was used to calibrate line position and shape. Both powder standard and the film and powder samples were analyzed under identical instrumental conditions as the

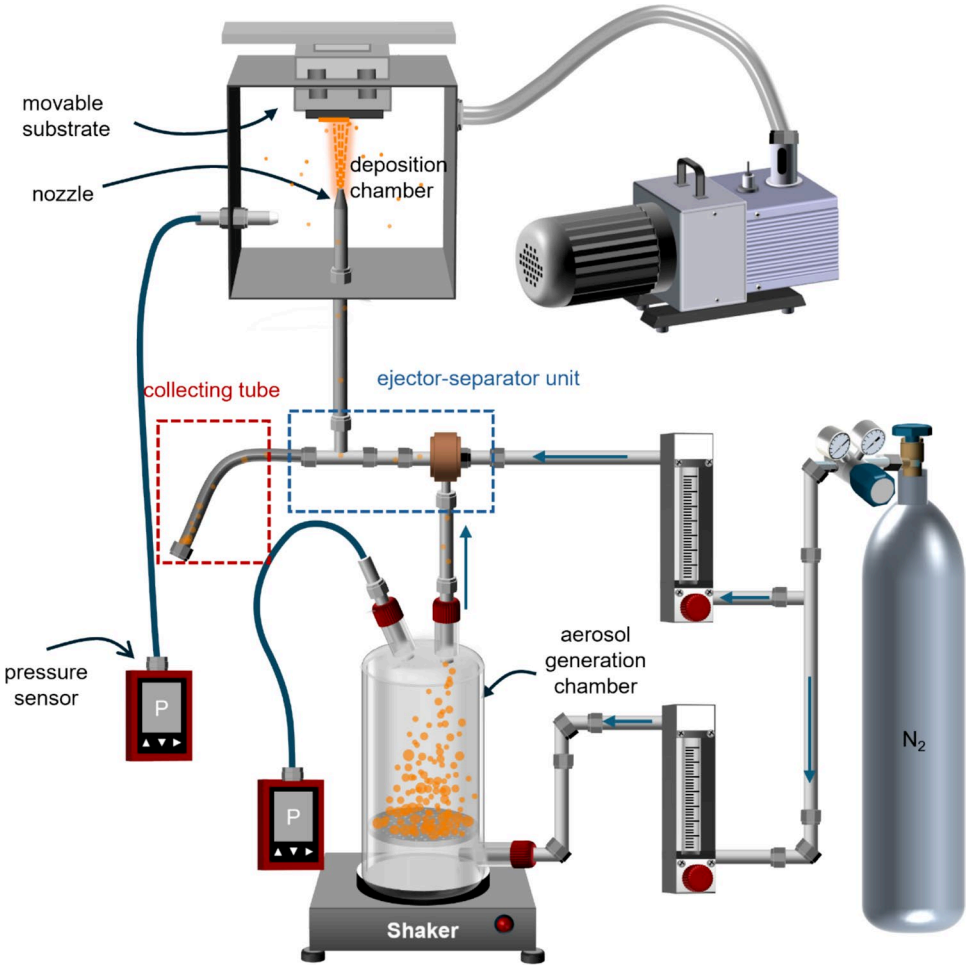

Figure 1 Schematic illustration of PAD setup with an ejector–separator unit and an inertial separator with a collecting tube.

film samples. The 2D diffraction patterns were then integrated at the beamline using a pyFAI script and reduced to 1D diffractograms.

The software TOPAS Academic 64 V7.24 (Cuhelo Software, Brisbane, Australia) was used for profile analysis. A full-profile analysis was performed to analyze phase purity. The microstructure was analyzed using a structure-independent Pawley fit [25], as this allowed for better agreement between the reflection shapes and intensities. A Thompson–Cox–Hastings pseudo-Voigt function [26] was utilized as the instrumental resolution function, whose parameters were determined based on the measurement of the NIST SRM 640 g standard. Reflection broadening was analyzed for the microstructure. This was done using the double Voigt approach according to Balzar [27], in which a Voigt-like shape is assumed for both size broadening and strain broadening. XRD patterns of the as-deposited and annealed $MAPbBr_3$ thin films were additionally acquired using a Bruker D8 Discover diffractometer equipped with Cu-Kα_1 radiation ($\lambda = 1.5418$ Å, a Ge (1 1 1) monochromator and a Lynxeye 1D detector (Si strip detector, 9 mm × 75 µm strip size), operating in Bragg–Brentano geometry. The measurements were taken with a step size of 0.020° over a 2θ range from 10° to 50°, using a counting time of 0.5 s per step, under ambient conditions. The X-ray source was operated at 40 kV and 40 mA.

The profile analysis of the measurements with the laboratory diffractometer was similar to those recorded at DESY. The only addition was the axial convolutions, which correct the asymmetrical line shapes due to the Bragg–Brentano setup with the 1D detector and the associated axial divergence.

Table 1 Experimental parameters for powder aerosol deposition of $MAPbBr_3$

Deposition Parameters	
Nozzle orifice	10 mm × 0.5 mm
Carrier gas	N_2
Gas flow rate (aerosol generation chamber)	0.13 L min^{-1}
Gas flow rate (Venturi)	8 L min^{-1}
Deposition chamber pressure	≈ 7 mbar
Aerosol generation chamber pressure	≈ 90–95 mbar
Nozzle–substrate distance	2–3 mm
Substrate scan speed	1 mm s^{-1}
Substrate scan distance	15–20 mm
Number of scans	2–30
Vibrating table	480 min^{-1}
Powder mass	0.8 g

Film thickness and surface roughness

The film thickness and surface roughness R_a of the aerosol-deposited films were measured using a profilometer (Dektak 150, Veeco).

Scanning electron microscopy

The powder and film morphology was characterized by scanning electron microscopy (SEM) using a Zeiss Leo Gemini 1530 instrument equipped with an In-lens detector and SE2 detector. An acceleration voltage of 3 keV for SE imaging was applied. All samples were coated with a conductive platinum layer with a thickness of approximately 2.6 nm.

Quasi-steady-state photoluminescence

For photoluminescence (PL) measurements, powder samples were placed in custom-made sample holders consisting of a glass slide with a cylindrical cavity, which was sealed with cover glasses (Th. Geyer) using parafilm. Film samples were measured as is under a N_2 atmosphere. Repeating the measurements under vacuum or in air yielded identical results. The samples were probed using an N_2 laser of type MNL 100 and manufacturer LTB, which emits 2.5 ns pulses of wavelength 337.1 nm. The laser was operated at a frequency of 20 Hz. The beam profile at the sample position had a circular top-hat shape with an effective area of 0.0255 cm^2. Neutral density filters were used to attenuate the laser beam to the desired fluence. In the optical detection path, a 355 nm long-pass filter (Thorlabs) was used to remove scattered excitation light. The photoluminescence was focused into a spectrograph (Andor Shamrock SR303i) and recorded with a Si CCD camera (Andor iDus DU420A OE). All spectra were corrected for detection efficiency of the setup.

Time-resolved photoluminescence

Time-resolved PL measurements were taken using the same samples as for the quasi-steady-state measurements in a home-built setup consisting of a temperature-controlled continuous flow helium cryostat (Oxford Instruments OptistatCF-X), a frequency-tripled Nd:YAG laser (Innolas SpitLight 600) with a wavelength of 355 nm, frequency of 100 Hz and pulse energy of 62.5 μJ as excitation source, and a spectrograph coupled to a gated intensified charge-coupled device (iCCD) camera (Andor iStar 334) for detection. The illumination spot at the sample position had a Gaussian shape with an area of 0.01 cm^2. Neutral density filters were used to attenuate the laser beam, resulting in a fluence of around 12 μJ/cm^2 at the sample position. The film samples were measured under helium atmosphere. Exponentially increasing delay and gating times were used to obtain the time-resolved spectra, with the delay times being kept about ten times longer than the gate times. To extract the intensity at each point in time, the background-subtracted PL spectra were integrated over the range of the emission peak, and the result was divided by the respective gate width.

Absorbance

To characterize the absorption of the powder and the thin-film samples under comparable conditions, diffuse reflectance spectra were recorded using a UV–Vis–NIR Spectrometer Cary 5000 (Varian) equipped with a DRA2500 integrating sphere. The samples were placed in powder cells, and the reflected intensity was measured using the built-in PMT detector. The recorded reflection data was divided by a reference measurement of a powder cell holder with Spectralon™ insert to calculate the reflectance spectrum $R(\lambda)$ of the sample. Assuming the measured reflectance of the thick samples is optically equivalent

to the reflectance of an infinitely thick sample, the Kubelka–Munk function $F(\lambda)$ can be applied [28]: $F(\lambda) = A(\lambda)/S(\lambda) = (1 - R(\lambda))^2/(2R(\lambda))$. Here, $A(\lambda)$ is the absorbance spectrum and $S(\lambda)$ the scattering, which we approximated as constant.

Impedance spectroscopy

Prior to electrical characterization, the aerosol-deposited $MAPbBr_3$ films were subjected to a post-deposition annealing process. As illustrated in Fig. S14, the samples were heated to 110 °C and maintained at this temperature for 2 h. After annealing, the samples were cooled down to room temperature (20 °C). Subsequently, a series of temperature-dependent impedance spectroscopy measurements were taken, with the temperature increased in steps of 10 °C from 20 to 110 °C. These measurements were taken with an Alpha-A high-performance frequency analyzer from the manufacturer Novocontrol Technologies. The frequency was swept from 1 MHz to 0.1 Hz with an effective voltage amplitude of 30 mV. No DC voltage was applied. The measurement was taken in darkness to exclude photoinduced effects. All impedance spectra at different temperatures were fitted using the RelaxIS software.

Results and discussion

In the following sections, we elaborate on the fabrication of $MAPbBr_3$ films by powder aerosol deposition (PAD) and discuss their microstructural, optical, and electrical properties.

From powder to film

For PAD, both the size of primary particles and the degree of agglomeration of powder are crucial, because they strongly influence particle acceleration and impact behavior. In general, only particles within an intermediate size range possess sufficient inertia to reach the substrate and contribute to film growth. Particles that are too small typically exhibit insufficient adhesion, whereas excessively large particles may cause damage to the substrate [28].

Figure 2 shows the SEM images of the milled $MAPbBr_3$ powder in different magnifications. At low magnification (Fig. 2a), the powder consists of agglomerates with sizes of several tens of micrometers. Higher magnification (Fig. 2b) reveals that these larger agglomerates are composed of faceted primary particles with $D_{50} = 1.07$ µm and $D_{90} = 1.24$ µm, where D_{50} denotes the median particle diameter at which 50% of the particles are smaller. This particle size is within the range generally considered suitable for PAD [29]. However, it is noticeably larger than the mean particle size of approximately 700 nm reported by Leupold for $MAPbI_3$ powder after the same milling time of 60 min [29].

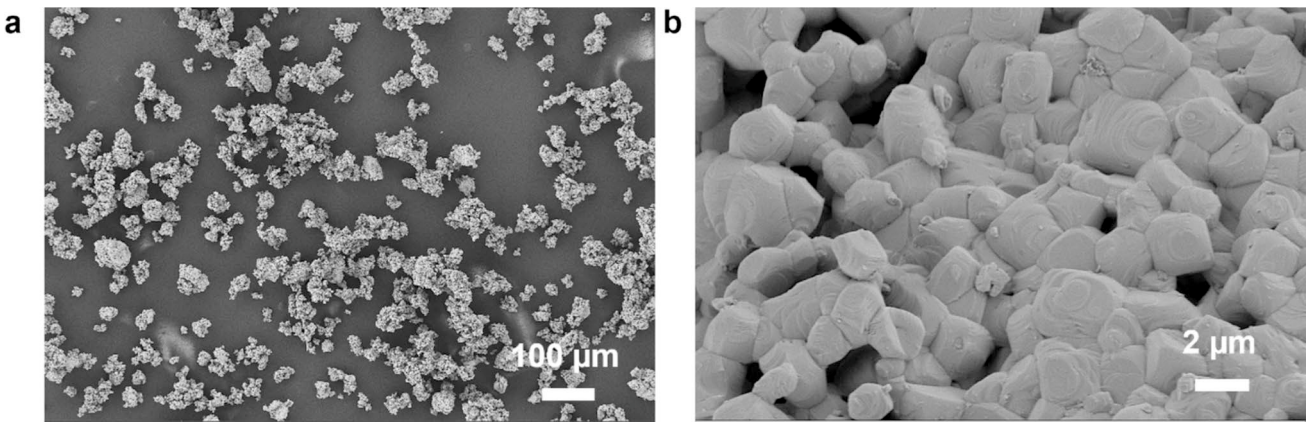

Figure 2 SEM images of the milled $MAPbBr_3$ powder in different magnifications: **a** an overview image showing the size of the agglomerates and **b** a detailed view showing the faceted morphology of the primary particles.

Besides the primary particle size, the agglomeration state—particularly the size and compactness of agglomerates—strongly affects the deposition behavior and, consequently, the quality of the deposited films. When deposition is carried out without an ejector–separator unit and an inertial separator equipped with a collecting tube (see SI Fig. S1), the resulting $MAPbBr_3$ film exhibits poor adhesion to the SnO_2-coated ITO glass substrate, as shown in the cross-sectional SEM image in Fig. 3a. In addition, the $MAPbBr_3$ films are highly inhomogeneous with weak interparticle bonding.

This behavior can be attributed to the presence of large agglomerates in the aerosol. Upon impact with the substrate, a substantial fraction of the kinetic energy of these agglomerates is dissipated through agglomerate breakup rather than contributing to the deformation and fracture of primary particles. Consequently, insufficient energy remains to induce effective room-temperature impact consolidation (RTIC). This loss of impact energy hampers particle bonding and typically results in porous microstructures and poorly adherent films, consistent with previous reports [19, 21].

To mitigate these issues, we employed an ejector unit combined with an inertial separator, as originally introduced by Biberger et al. [21]. In this setup, the aerosol leaving the flask is accelerated by a high-velocity gas stream in the ejector. At the point where the acceleration flow intersects with the aerosol flow, strong shear forces arise, as shown in Fig. 1. These shear forces can break up weak agglomerates before they reach the separator. In addition, the ejector also allows independent control of the aerosol flow rate V_{flask} and the acceleration flow V_{acc}. After the ejector, the aerosol passes through an inertial separator, where the gas flow is deflected by 90°. Small powder particles and weak agglomerates can follow the gas stream toward the slit nozzle, whereas large agglomerates are not deflected due to their higher inertia and collected in a collecting tube.

However, the PAD process parameters optimized for $MAPbI_3$ by Leupold et al. [29] cannot be directly applied to $MAPbBr_3$, as the more compact agglomerates of $MAPbBr_3$ require more effective aerodynamic deagglomeration. To address this, the gas flow rate in the aerosol generation chamber was reduced from 0.25 to 0.13 L min^{-1}, and the powder mass was decreased from 1 to 0.8 g. Therefore, the particle flux in the aerosol stream was reduced, thereby enhancing deagglomeration and inertial separation and enabling the formation of uniform, dense, and well-adherent $MAPbBr_3$ films, as shown in Fig. 3b.

In addition, under these optimized deposition parameters, the film thickness can be controlled by adjusting the number of scans, ranging from approximately 2 to 50 µm, as shown in Table 2. This thickness range is broader than those reported in previous PAD studies on halide perovskites. For instance, Leupold et al. reported $MAPbI_3$ films of 20–40 µm using N_2 as the carrier gas, whereas thinner films of only a few micrometers required He [29]. Similarly, These et al. obtained $CsPbBr_3$ films with thicknesses of 20–35 µm using N_2 [23].

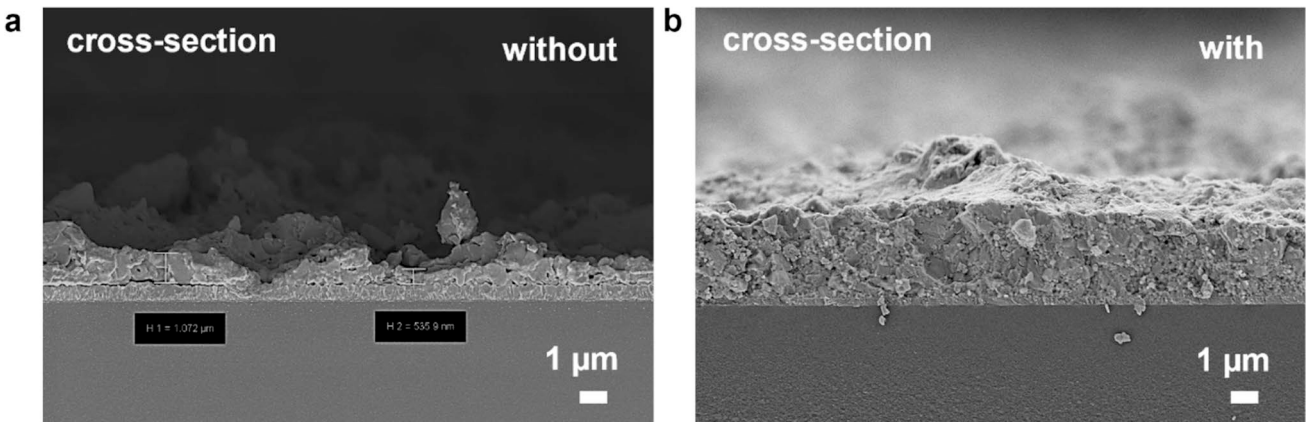

Figure 3 SEM images of the aerosol-deposited $MAPbBr_3$ films on SnO_2-coated ITO glass substrates **a** without ejector–separator unit and inertial separator **b** with ejector–separator unit and inertial separator.

Table 2 Film thickness of $MAPbBr_3$ deposited with different scan numbers on two substrates: SnO_2-coated ITO and C-IDEs patterned Al_2O_3 substrates

Substrate	Number of scans	Film thickness/μm
SnO_2/ITO	2	2.6 ± 0.9
	20	28.5 ± 5.6
	30	43.2 ± 7.9
C-IDE/Al_2O_3	2	2.9 ± 1.3
	20	30.9 ± 4.7
	30	44.8 ± 6.9

Such perovskite films with thicknesses exceeding 50 μm are essential for applications requiring large absorber volumes, particularly in radiation detectors [30, 31], where the weak interaction of X-rays with the absorber necessitates sufficiently thick layers for efficient detection [32]. However, conventional solution-based methods, such as spin or blade coating, often struggle to achieve the required thickness (> 10 μm) due to evaporation-induced surface crystallization and crack formation [33]. In this regard, PAD offers a promising solvent-free alternative. Its ability to produce dense $MAPbBr_3$ films with tunable thicknesses, ranging from a few to several tens of μm, highlights its significant potential for radiation detection applications.

Structural and microstructural characterization

A remarkable feature of our aerosol-deposited $MAPbBr_3$ films is the pronounced grain size reduction that occurs during deposition. The originally micron-sized $MAPbBr_3$ powder particles are transformed into sub-micrometer fragments upon high-velocity impact. This significant reduction in size is a clear indication of particle fracture and plastic deformation, representing a key signature of the RTIC mechanism that governs PAD [19].

Figure 4 shows the cross-sectional and top-view SEM images of the aerosol-deposited $MAPbBr_3$ films

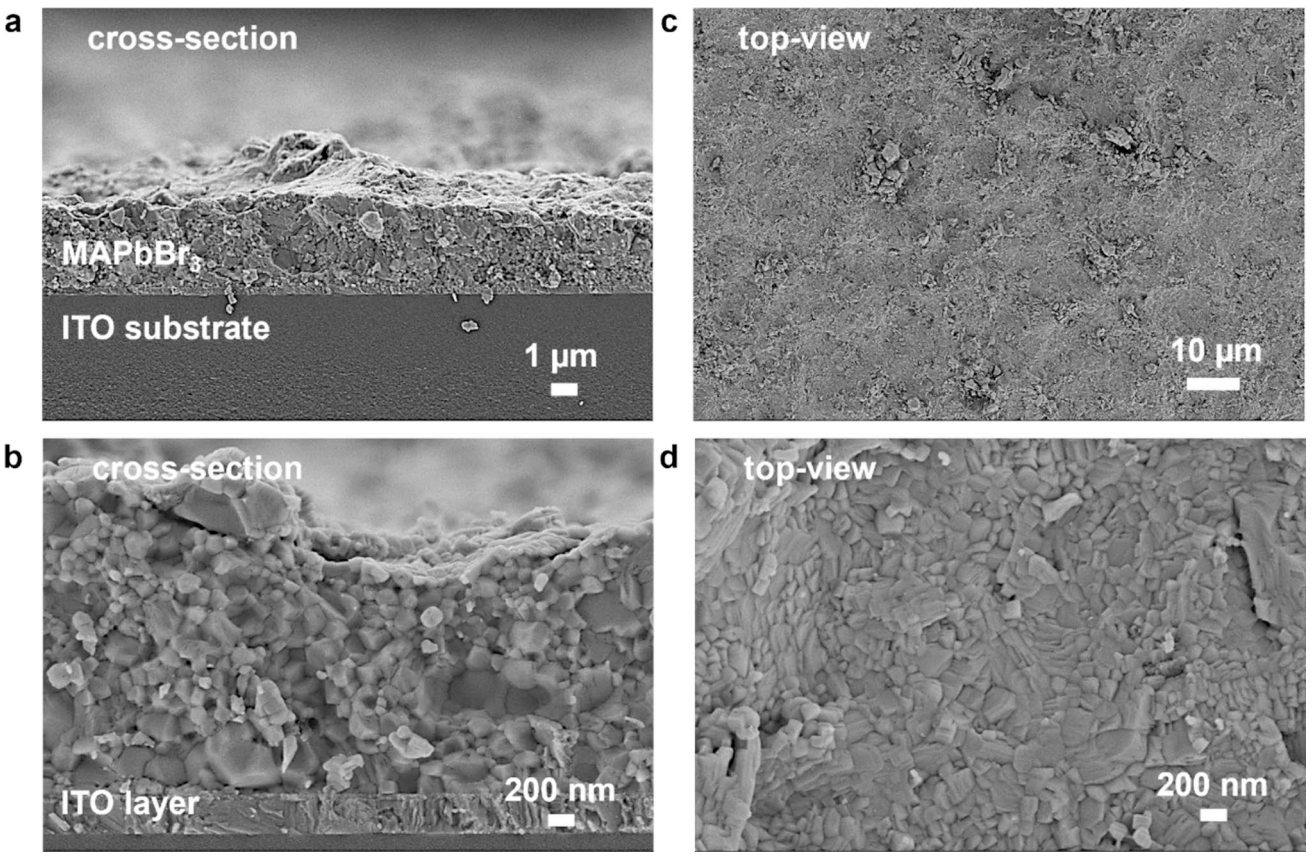

Figure 4 SEM images of the aerosol-deposited $MAPbBr_3$ films on SnO_2-coated ITO glass substrates in different magnifications: **a** and **b**: fractured cross section, **c** and **d**: top view.

in different magnifications. The cross section (Fig. 4a) exhibits a uniform thickness of approximately 2.5 µm with an interface to the underlying SnO_2-coated ITO glass substrate. The film is compact and continuous across the entire cross section. No visible delamination or large voids are observed, confirming the mechanical integrity of the $MAPbBr_3/SnO_2$ interface. As shown at high magnification in Fig. 4b, the $MAPbBr_3$ film consists of sub-micrometer grains, much smaller than the primary particles in the milled powder (Fig. 2b), consistent with the impact induced fragmentation described above. The top view (Fig. 4c and Fig. 4d) shows a rough but continuous surface morphology composed of closely packed fragments. Such surface features are typical for RTIC and arise from particle fragmentation and rearrangement upon impact rather than surface damage. No macroscopic cracks or pinholes are apparent, indicating homogeneous surface coverage over large areas.

Figure 5a, b shows the X-ray diffraction (XRD) patterns of $MAPbBr_3$ powder and $MAPbBr_3$ film deposited on an ITO-coated glass substrate, respectively. The XRD pattern of the $MAPbBr_3$ powder indicates a cubic crystal structure with space group $Pm\bar{3}m$ and a lattice parameter of $a = 5.933$ Å, which is in agreement with the reported literature value ($a = 5.933$ Å) [34]. After deposition, the $Pm\bar{3}m$ crystal structure is retained, with a lattice parameter of $a = 5.934$ Å. No secondary crystalline phases such as MABr or $PbBr_2$ are detectable, indicating that the PAD process does not induce phase decomposition. The aerosol-deposited $MAPbBr_3$ film exhibits a relatively low microstrain value of 0.003% and a crystallite size of (89.8 ± 19.1) nm, indicating nanoscale crystallites. In contrast, the crystallite size of the powder is in the micrometer range (i.e., beyond the resolution limit of line-broadening analysis).

Optical properties (Absorption, PL, TRPL)

To complement the structural characterization, we compared the optical properties of a ball-milled $MAPbBr_3$ powder used for powder aerosol deposition with those of the resulting films. The films exhibit homogeneous optical characteristics across each sample and show good reproducibility when fabricated under identical conditions (see SI Fig. S4). Figure 6a presents the absorbance spectra—derived from reflectance measurements—of the powder and a representative film with a thickness of approximately 5 µm. Both samples display nearly identical absorption edges at 2.29 eV as extracted from Tauc plots (see also SI Fig. S5). These values are consistent with previously reported values for $MAPbBr_3$ [35]. We note that the Tauc-derived values should be regarded as empirical descriptors of the absorption onset, as the electronic bandgap is likely underestimated due to non-negligible excitonic contribution to absorption in this material. We attribute the slight differences between film and powder spectra to substrate-related scattering/reflection.

In contrast to the absorbance spectra, the photoluminescence (PL) spectra of the powder and film (Fig. 6b) reveal pronounced differences. The main

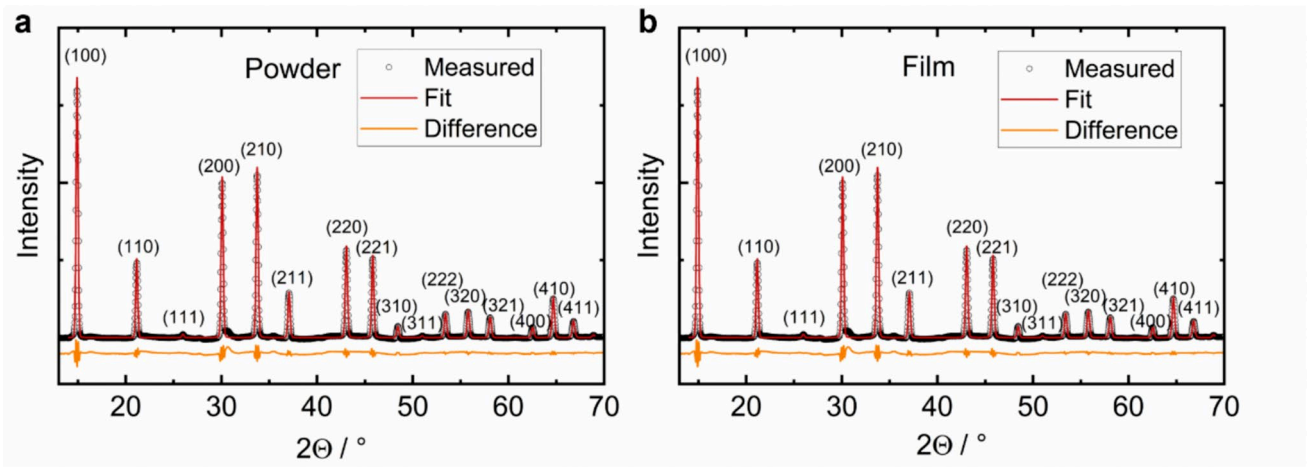

Figure 5 Rietveld refinement results of X-ray diffraction patterns for **a** the as-processed powder and **b** the aerosol-deposited $MAPbBr_3$ film.

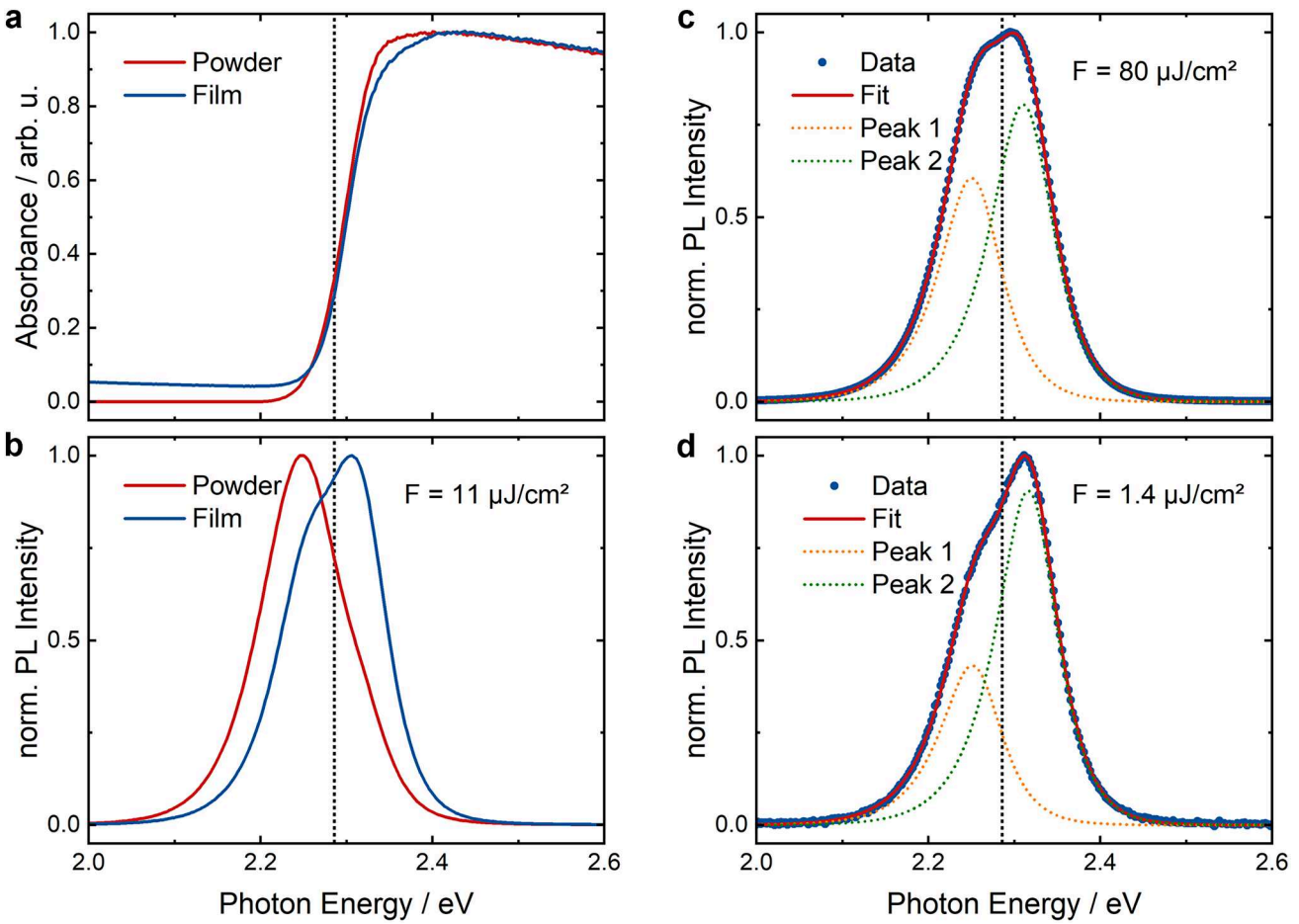

Figure 6 **a** Absorbance spectra derived from reflectance measurements and **b** PL spectra of a $MAPbBr_3$ powder and film, both recorded under a fluence of 11 μJ/cm^2. The right side shows the deconvoluted PL spectra of the film under **c** high and **d** low fluence**.** The horizontal dotted black lines indicate the Tauc-derived absorption onset at 2.29 eV.

emission peak of the film (at 2.32 eV) is blueshifted relative to the main peak of the powder (at 2.25 eV) by approximately 70 meV. Both spectra display structured emissions, though with distinct characteristics. The film shows a pronounced low-energy shoulder (at 2.26 eV), while the powder displays a weaker high-energy shoulder (at 2.31 eV). These shoulders are more clearly visible in semilogarithmic representation and the derivative plot, which are provided in Fig. S6. Notably, the high-energy features of the PL extend to energies above the Tauc-derived absorption onset (dotted line), consistent with observations reported previously for aerosol-deposited $CsPbBr_3$ films [23].

To further examine these spectral features, emission spectra were collected at varying excitation fluences, with exemplary measurements for the film shown in Fig. 6c, d (see SI Fig. S7 for all fluences and Fig. S9 for powder measurements). Although the overall spectral shape remains consistent across fluences, the high-energy feature becomes markedly more pronounced at lower excitation intensities. To parameterize this systematic change in line shape, we fitted the spectra using two components, a lower-energy peak and a higher-energy peak. Details of the deconvolution procedure and the corresponding fitting parameters for different fluences are provided in SI Sect. S2. The lower-energy peak is located at approximately 2.25 eV for the powder and 2.26 eV for the film, and its position remains essentially independent of excitation fluence (Fig. 6c, d, Fig. S10). The higher-energy peak appears at roughly 2.31 eV for the powder and 2.32 eV for the film, and in both cases exhibits a slight redshift with increasing fluence. As noted above, the relative contribution of the lower-energy component increases with excitation fluence for both sample types (Fig. 6c, d, Fig. S10).

Similar multi-component emission behavior has previously been reported for $MAPbBr_3$, and several mechanisms have been proposed, including self-absorption processes [36, 37], simultaneous recombination of bound excitons and free carriers [38, 39], radiative recombination via defects (e.g., surface states) [40, 41], and phenomena such as Rashba-like spin splitting [42].

In our samples, the higher-energy emission peak lies 20–30 meV above the onset of absorption, suggesting that the measured absorption edge corresponds to an excitonic transition rather than the intrinsic bulk bandgap. We therefore attribute the higher-energy emission near 2.32 eV to radiative recombination of free carriers occurring close to the bulk bandgap energy, whereas the lower-energy peak is likely associated with either self-absorption effects, emission from defects, or radiative recombination of bound excitons.

The increasing relative contribution of the lower-energy peak at higher charge-carrier densities points against a defect-based interpretation, since defect emission would be expected to saturate as the available states become filled. At the same time, several observations are difficult to reconcile with a purely excitonic origin. Specifically, the relative intensities of the two peaks differ significantly between the powder and the film, and the position of the lower-energy peak varies with film thickness (see SI Fig. S12).

These effects are characteristic for self-absorption processes, indicating that self-absorption contributes significantly to the observed spectral features. Nevertheless, the increase of the lower-energy contribution with excitation fluence is not readily explained by a simple self-absorption-only picture. We therefore conclude that self-absorption is an important factor in determining the observed PL line shape, while a complete quantitative description of the dual-emission behavior remains beyond the scope of the present work.

To assess the defect properties of the aerosol-deposited films, time-resolved photoluminescence (TRPL) measurements were taken. The PL decay of a representative film (Fig. 7) is well described by a simple rate equation model (red curve), which assumes that radiative recombination is dominated by free carriers and that the carrier dynamics are influenced by a single effective shallow trap state. A comparable modeling approach has been employed by Yuan et al. [43] for a triple-cation perovskite film. Additional details on the

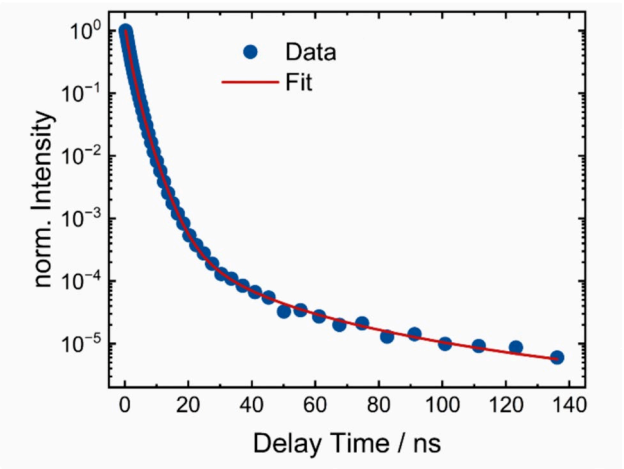

Figure 7 PL decay of a thin film measured under a fluence of 12 μJ/cm^2. The red line indicates a fit to the data according to a rate equation model detailed in SI Sect. S3.

recombination model and the corresponding fitting parameters are provided in SI Sect. S3. From the fit, we obtain a trap density of $N_T = 1.6 \times 10^{18}$ cm^{-3}, which is higher than values typically reported for solution-processed thin films [44–46].

This elevated defect density is likely a consequence of the deposition process. In metal halide perovskites, grain surfaces and grain boundaries are often dominant sources of non-radiative recombination [40]. In the present case, the small crystallites in the film exhibit a high surface-to-volume ratio and may additionally contain defect-rich grain surfaces generated by the fracturing of larger powder particles during deposition.

PL-based measurements are inherently weighted toward the optically excited near-surface region of the film. The extracted N_T should therefore be regarded as an effective trap density of the TRPL-probed region rather than as a purely bulk quantity. In particular, the topmost region of the film may contain a higher defect density than deeper layers, since, unlike the lower part of the film, it does not undergo further compression and restructuring during subsequent particle deposition. We note that the surface sensitivity of PL is especially relevant when additional external interface-specific recombination pathways are present [47, 48]. In our case, however, we do not expect a significant contribution from such distinct interface-induced channels at the free film surface in helium, and the

measured decay is already well captured by a model containing only band-to-band recombination and a single effective trap state.

Overall, the optical properties of the aerosol-deposited films closely resemble those of the precursor powder, with similar absorption onsets and structured emission spectra. However, some notable differences are observed. Most prominently, the relative intensities of the two emission peaks vary substantially: While the lower-energy peak dominates the emission of the powder, the higher-energy peak is more intense in the film. This contrast may be attributed to reduced self-absorption in the film geometry relative to the powder. In addition, TRPL measurements indicate a high trap density in the film compared to typical solution-processed films, consistent with the influence of the deposition process. One potential strategy to reduce the defect density would be to employ post-deposition treatments such as hot pressing, which has been shown to improve the quality of aerosol-deposited $MAPbI_3$ films [49].

Electrical and transport properties

To further characterize the films, temperature-dependent impedance spectroscopy was employed to investigate their electrical transport properties. Although initial structural characterization was performed on SnO_2-coated ITO glass substrates, neither SnO_2 nor commonly used oxide electrodes such as ITO can be considered as ideal ion-blocking contacts. Previous studies have demonstrated that interfacial instabilities, including oxygen vacancy-mediated halide migration at the perovskite/SnO_2 interface [50, 51] and electric field-driven atomic intermixing at the perovskite/ITO interface [52], can complicate the interpretation of impedance spectra. To mitigate these effects, symmetric carbon interdigitated electrodes on insulating Al_2O_3 substrates were employed. Carbon is relatively inert toward halide perovskite materials, thereby providing a closer approximation to ion-blocking conditions and reducing interfacial reactions during measurements.

To facilitate comparison, we used identical aerosol deposition parameters to fabricate $MAPbBr_3$ films on both substrates. Although substrate properties such as surface roughness and hardness may influence film formation during PAD, cross-sectional SEM images (Figs. S2 and S3) confirm that the films on both substrates exhibit comparable thicknesses, similar nanocrystalline microstructures, and continuous interfaces without delamination. These observations support the comparability of the structural and electrical analyses performed on the two substrate configurations.

It is well established that $MAPbBr_3$ films undergo thermal decomposition when annealed at temperatures exceeding approximately 180 °C [53]. To avoid unintended in situ annealing and the associated grain growth during temperature-dependent impedance measurements, the films were pre-annealed at the maximum measurement temperature (110 °C) for 2 h under a nitrogen atmosphere. The full measurement protocol is depicted in Fig. S14. SEM analysis (Fig. S15) shows that this treatment induces an observable increase in grain size. Furthermore, XRD analysis (Fig. S16) shows that there is no indication of phase degradation. Temperature-dependent impedance measurements were taken to investigate the charge transport, relaxation dynamics, and the underlying conduction mechanisms in the annealed PAD-$MAPbBr_3$ films. Figure 8 shows the temperature-dependent impedance spectra of the annealed PAD-$MAPbBr_3$ films measured from 293 to 383 K.

The frequency dependence of the real part of the impedance (Z') measured at various temperatures is shown in Fig. 8a. In the high-frequency region, the Z' curves measured at different temperatures start from nearly the same value of 1.5×10^4 Ω. As the frequency decreases, the curves gradually separate. Since the measurements were taken under dark conditions, the contribution from photogenerated electronic carriers can be neglected. Moreover, the direct contact between $MAPbBr_3$ and carbon forms a Schottky interface [54]. Such an interfacial barrier effectively suppresses intrinsic electronic transport. The low-frequency impedance results, as discussed in SI Sect. S5 and shown in Fig. S17a, further indicate that the ionic contribution exceeds the electronic contribution by more than one order of magnitude. As a result, the measured response is considered to be predominantly governed by ionic transport. In the low-frequency region, Z′ reaches a plateau that exhibits a strong temperature dependence, with lower values observed at higher temperatures. This behavior is consistent with thermally activated ionic transport.

Figure 8b presents the frequency dependence of the imaginary part of the impedance ($-Z''$). As the frequency decreases, $-Z''$ increases and reaches a

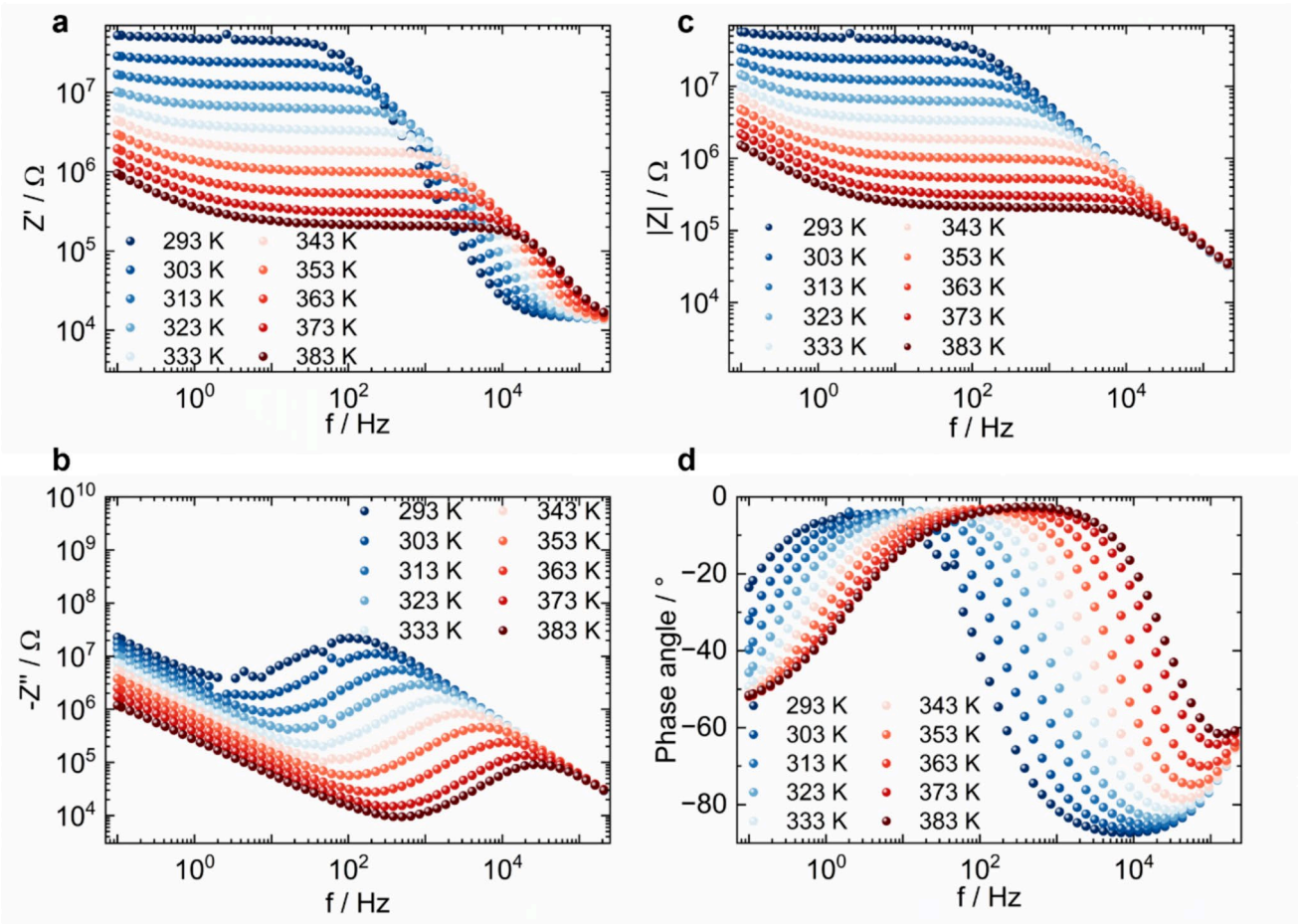

Figure 8 Temperature-dependent impedance spectroscopy of annealed $MAPbBr_3$ film measured in the dark. **a** Real part of the impedance Z′, **b** imaginary part of the impedance Z″, **c** impedance magnitude |Z|, and **d** phase angle as a function of frequency.

local maximum, which is associated with the space charge relaxation in the bulk. At lower frequencies, − Z″ reaches a minimum before showing an upward trend, marking the onset of electrode polarization. With increasing temperature, the peak frequency shifts toward higher values, indicating accelerated relaxation dynamics.

Figure 8c shows the impedance magnitude |Z| as a function of frequency. In the high-frequency region, the spectra converge, while they diverge significantly in the low-frequency region, where the magnitude decreases with rising temperature, consistent with the thermally activated nature of the system. Figure 8d shows the phase angle as a function of frequency. In the high-frequency region, the phase angle is around − 60°, indicating a mixed resistive–capacitive response. As the frequency decreases, the phase angle approaches values closer to 0°, suggesting a stronger resistive contribution. In the low-frequency region, the phase angle becomes more negative again, reflecting the increasing influence of electrode polarization caused by ionic accumulation at the electrode interfaces.

Figure 9a shows the Nyquist plots measured over the temperature range from 293 to 383 K. At all temperatures, the impedance spectra consist of a semicircular arc in the high- and mid-frequency regions, followed by a low-frequency tail associated with ion blocking. The radius of the semicircle decreases significantly with increasing temperature, indicating a reduction in the overall resistance and reflecting thermally activated ionic transport. The presence of only one arc suggests overlapping contributions from grain interior and grain boundary processes. However, as shown in Fig. 9b, the real capacitance exhibits a frequency-independent plateau of $C' \approx 2.7 \times 10^{-11}$ F, which indicates that the measured response is mainly associated with the grain interior contribution for films [55].

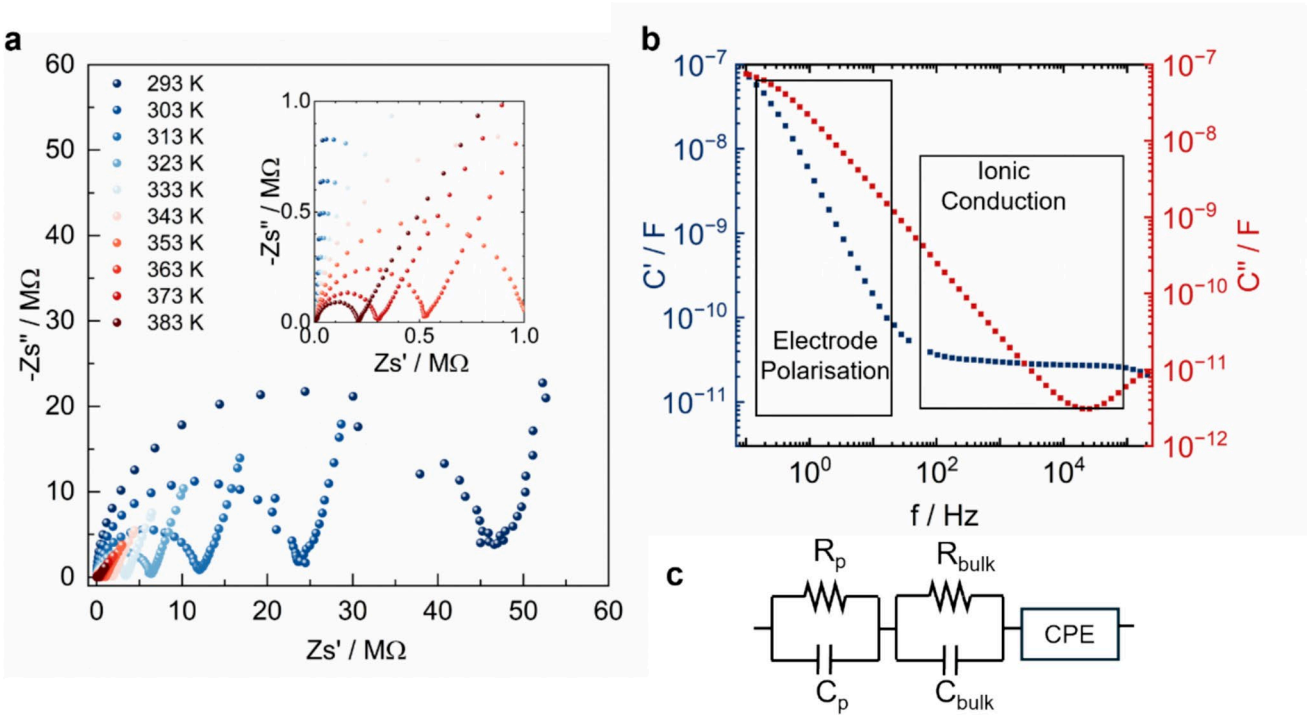

Figure 9 Temperature-dependent impedance spectroscopy of an annealed $MAPbBr_3$ film measured in the dark. **a** Nyquist plots of the complex impedance. The inset shows a magnified view of the low-impedance region. **b** Frequency dependence of the real (C′) and imaginary (C″) capacitance of $MAPbBr_3$ at 323 K. **c** Equivalent circuit model used to fit the impedance spectra, consisting of two Voigt elements and a constant phase element (CPE).

According to the classical brick layer model, the grain interior and grain boundary contributions can only be experimentally resolved when their associated RC time constants differ sufficiently, typically by at least one order of magnitude [56, 57]. Since grain boundary capacitance scales with the ratio of grain interior to grain boundary thickness (as shown in Eq. 1) [55], larger grain sizes therefore tend to allow for a clearer separation of the two contributions. In our case, however, due to the small grain size (~ 90 nm) and the resulting overlap of their characteristic time constants, the individual contribution of grain interior and grain boundary cannot be distinguished in the impedance spectra. Furthermore, the real part of the capacitance continuously increases with decreasing frequency which is characteristic of electrode polarization at low frequencies [55].

$$C_{gb} = \frac{l_{gi}}{l_{gb}} \cdot C_{gi} \tag{1}$$

To quantitatively describe the impedance response, the experimental data were fitted using an equivalent circuit model based on the Voigt model. As shown in Fig. 9c, the model consists of two Voigt elements in series combined with a constant phase element (CPE) accounting for electrode polarization effects in the low-frequency region. The first R‖C element is used to describe fast responses associated with parasitic resistive and capacitive contributions in the high-frequency measurement setup. As previously mentioned, due to the small grain size, the second R‖C element is used to describe the combined charge transport contributions from both the grain interior and grain boundary within the $MAPbBr_3$ film. A more detailed discussion of the physical assignment of the individual elements in this equivalent circuit is provided in SI Sect. S5. As SI Fig. S20 and Fig. S21 show, the equivalent circuit model reproduces the experimental impedance spectra well, indicating that the chosen model adequately describes the electrical response of the system.

According to Eqs. S10, S11, the in-plane conductivity σ_{bulk} was determined to be 5.09×10^{-9} S cm^{-1} at 293 K. The conductivity increases with increasing temperature, reaching 1.15×10^{-6} S cm^{-1} at 383 K. (Detailed calculation is provided in SI Sect. S5.)

As discussed above and shown in SI Sect. S5, the ionic contribution exceeds the electronic contribution by more than one order of magnitude. Therefore, the in-plane conductivity σ_{bulk} is considered to be predominantly governed by ionic transport, i.e., $\sigma_{bulk} \approx \sigma_{ion}$.

While the equivalent circuit analysis provides access to conductivity, further insight into the dissipative nature of ionic transport can be obtained by analyzing the dielectric response. For instance, the loss tangent tanδ can quantify the dissipative component of the dielectric response. To describe the frequency-dependent electrical behavior, including relaxation phenomena, the dielectric response was expressed in terms of the complex permittivity, as given by Eq. 2. Under consideration of the empty capacitance of the substrate as well as the fact that the film thickness does not necessarily correspond to the effective electric field penetration depth in the IDE geometry, the real part (ε') and the imaginary part (ε'') of the complex permitivity are calculated according to Eqs. 3a, 3b. F_{geo} denotes the geometrical factor, and $C_{corr}\prime(\omega)$ is the corrected capacitance. The detailed derivation of these expressions is provided in SI Sect. S5. The loss tangent, tanδ, was determined according to Eq. 4.

$$\varepsilon(\omega) = \varepsilon'(\omega) - j\varepsilon''(\omega) \tag{2}$$

$$\varepsilon'(\omega) = 1 + \frac{C'_{corr}(\omega)}{\varepsilon_0 F_{geo}} \tag{3a}$$

$$\varepsilon''(\omega) = \frac{C''_{corr}(\omega)}{\varepsilon_0 F_{geo}} \tag{3b}$$

$$\tan\delta = \frac{\varepsilon''}{\varepsilon'} \tag{4}$$

As shown in Fig. 10a, clear relaxation peaks are observed in the loss tangent. This behavior arises from the frequency-dependent response of mobile ionic species. At high frequency ($\omega \gg \tau^{-1}$), ionic species are unable to follow the rapid field oscillations and are confined to localized oscillatory motion, representing the intrinsic bulk response. As the frequency decreases, mobile ions progressively drift over longer distances, leading to enhanced dissipation associated with ionic transport. At very low frequency ($\omega \ll \tau^{-1}$), the ions accumulate at the electrode interfaces, creating space charge polarization. Importantly, the relaxation peak coincides with the onset of the low-frequency tail in the Nyquist plot, indicating a crossover from the bulk-dominated response to the electrode polarization.

With increasing temperature, the peak intensity tanδ increases and the peak frequency f_p shifts toward higher frequencies, reflecting a thermally activated decrease in the relaxation time τ. This behavior

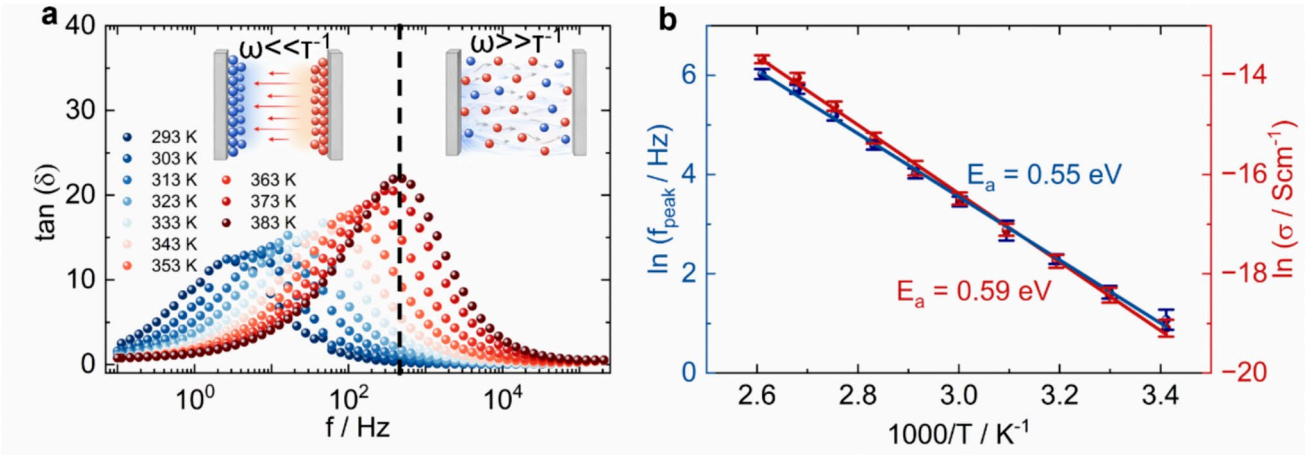

Figure 10 **a** Temperature-dependent dielectric loss tangent of an annealed $MAPbBr_3$ film measured in the dark at temperatures ranging from 293 to 383 K. **b** Arrhenius plots of the relaxation peak frequency f_p and the ionic conductivity σ_{ion} as a function of the inverse temperature. The error bars represent the combined uncertainty associated with the fitting procedure and an estimated instrumental error of approximately 5%.

is consistent with ionic relaxation. As temperature increases, the ionic mobility increases, thus enabling faster ionic redistribution under the alternating electric field. Since τ is inversely proportional to f_p according to Eq. 5a, the kinetics of this relaxation process can be quantitatively evaluated from the temperature dependence of f_p. Consequently, Arrhenius analyses were performed using Eqs. 5b, 5c to determine the activation energies E_a for both ionic conductivity and the dielectric relaxation process.

$$\tau = \frac{1}{2\pi f_p} \tag{5a}$$

$$\ln \sigma_{ion} = \ln \sigma_0 - \frac{E_a}{k_B} \cdot \frac{1000}{T} \tag{5b}$$

$$\ln f_p = \ln f_{p,0} - \frac{E_a}{k_B} \cdot \frac{1000}{T} \tag{5c}$$

Figure 10b shows the Arrhenius plots of the relaxation peak frequency f_p and the ionic conductivity σ_{ion} as a function of inverse temperature. Both exhibit linear behavior, with activation energies of approximately 0.55 eV for relaxation and 0.59 eV for ionic conductivity, respectively. The similarity of these activation energies suggests that the relaxation process and the ionic conductivity are governed by the same thermally activated ionic transport mechanism. Although the low-frequency response originates from electrode polarization, the kinetics of charge accumulation at the electrode interface are most likely dominated by bulk ionic transport rather than by interfacial reaction processes.

For comparison, the activation energies obtained for $MAPbBr_3$ in this work are slightly higher than the 0.4–0.5 eV reported by Leupold et al. for aerosol-deposited $MAPbI_3$ films [29]. This observation is consistent with the superior intrinsic stability of $MAPbBr_3$ compared to $MAPbI_3$. For a system at thermodynamic equilibrium, ionic conductivity is given by the product of mobile ion concentration and ionic mobility. Since both the ion concentration and mobility show Arrhenius-related temperature dependence, the activation energy extracted from conductivity measurements includes contributions from both mobile ion formation and ion migration [58, 59]. In halide perovskites, halide interstitials (X_i') or halide vacancies ($V_X^{\bullet}$) are typically considered to be the most readily formed and most mobile ionic species on the timescale of experiments [60–62]. The activation energy obtained in this work is consistent with reported bromine vacancy formation energy in $MAPbBr_3$ in the range of 0.4 eV–0.6 eV, which is generally higher than the iodine vacancy formation energy reported for $MAPbI_3$ [63]. This suggests that halide vacancy formation has a significant contribution to the overall activation energy in this system.

Nevertheless, in mixed ionic–electronic conductors such as halide perovskites, the redistribution of mobile ions is accompanied by a rapid electronic response [62, 64]. Therefore, although the observed relaxation is likely dominated by ionic dynamics, the contribution of ionic–electronic coupling cannot be completely neglected.

In addition to the activation energy, a quantitative description of ionic transport requires knowledge of both the diffusion coefficient and the mobility of the mobile species, as these parameters govern charge transport under an applied electric field. Previous studies have demonstrated that using the Trukhan model, the ionic diffusion coefficient can be extracted from the analysis of relaxation processes in impedance spectroscopy measurements [65–68].

The Trukhan model describes the dielectric response of conducting dielectrics, in which the impedance is primarily governed by ionic electrodiffusion and interfacial polarization [69]. The model is based on a linearized Nernst–Planck approach and assumes linear response, a homogeneous conducting medium and blocking interfaces. In the present $MAPbBr_3$–carbon system, the small AC perturbation amplitude (0.03 V) ensures operation within the linear regime, while the carbon electrode acts as an effectively ion-blocking contact, promoting ionic accumulation at the perovskite/carbon interface. Due to the small crystallite size (~ 90 nm), ion transport occurs through a highly interconnected network of grain interior and grain boundary. Consequently, the impedance response represents a macroscopic collective response of the film and is analyzed within an effective medium approximation. Therefore, the Trukhan model can be employed to estimate the diffusion coefficient from the relaxation process observed in the tan δ spectrum [68–71]. The diffusion coefficient of the dominant mobile ionic species can be estimated using Eq. 6. Here, L is the finger distance and $\omega_{max}^{\tan\delta}$ is the angular frequency corresponding to the maximum of the loss tangent, and $\tan(\delta)_{max,\omega}$ represents the loss

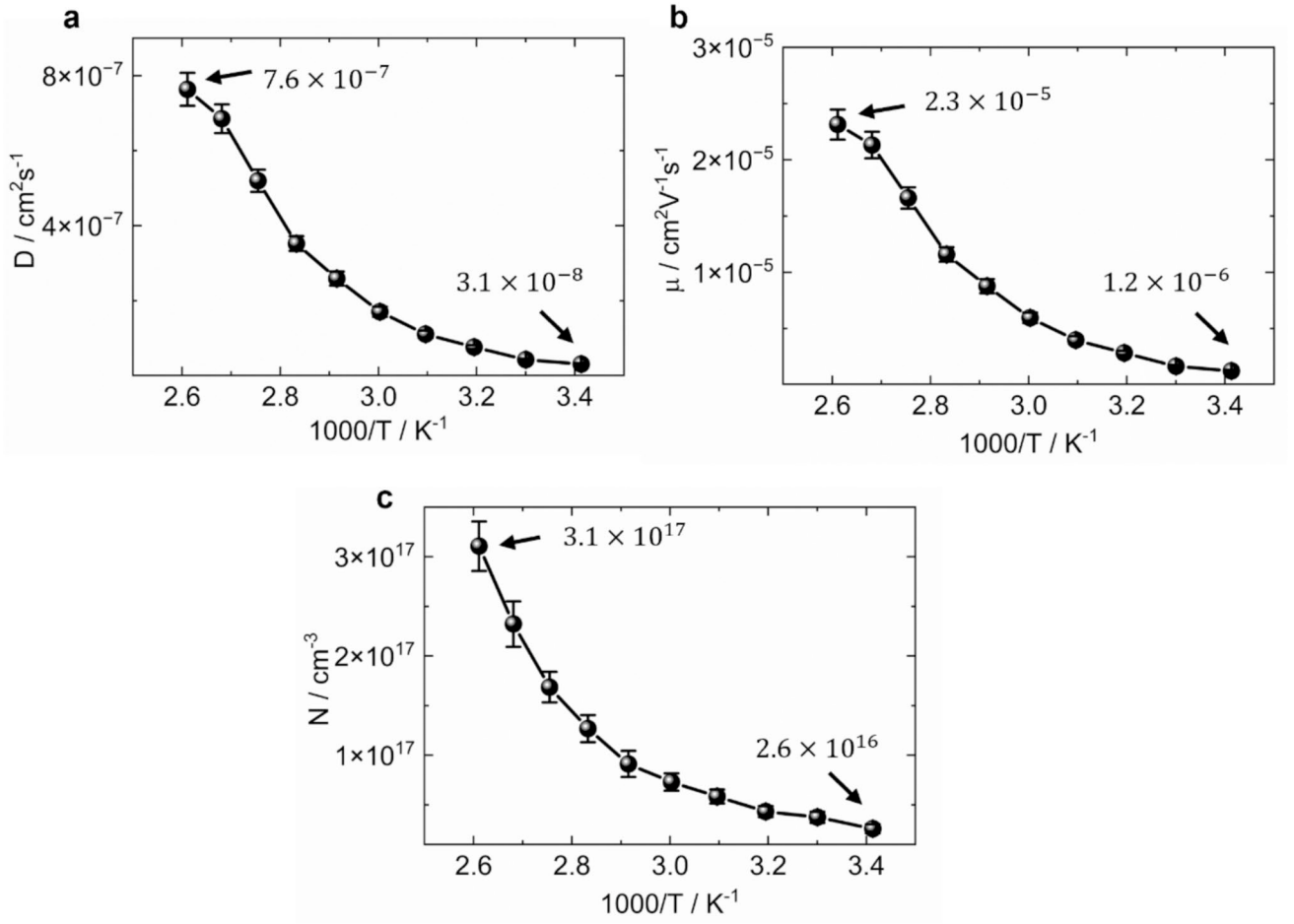

Figure 11 Temperature-dependent behavior of **a** diffusion coefficient D and **b** the carrier mobility μ derived from applying the Nernst–Einstein relation and **c** the ion concentration N_{ion}. Error bars for D include fitting and instrumental uncertainties (5%), whereas those for μ and N_{ion} were obtained by standard error propagation.

tangent at this frequency. A detailed derivation is provided in SI Sect. S6.

$$D = \frac{\omega_{max}^{\tan\delta} \cdot L^2}{32\left(\tan^3\delta\right)_{max,\omega}} \tag{6}$$

Figure 11a shows the temperature dependence of the diffusion coefficient extracted from the loss tangent spectra. The diffusion coefficient D increases with increasing temperature, from 3.1×10^{-8} cm^2 s^{-1} at 293 K to 6.8×10^{-7} cm^2 s^{-1} at 383 K. The extracted diffusion coefficients are consistent with literature values reported for bromide vacancy migration in $MAPbBr_3$ (10^{-8}—10^{-10} cm^2 s^{-1}) [72–77]. The corresponding ionic mobility μ was calculated using the Nernst–Einstein relation:

$$\mu = \frac{qD}{k_B T} \tag{7}$$

where k_B is the Boltzmann constant, T is the temperature, and q is the charge of a monovalent cation. The ionic mobility increases with temperature from 1.2×10^{-6} cm^2 V^{-1} s^{-1} at 293 K to 2.3×10^{-5} cm^2 V^{-1} s^{-1} at 383 K, as shown in Fig. 11b. This mobility value is of the same order of magnitude as reported ionic mobilities and is significantly lower than the electronic mobility [73]. With the ion mobility μ and knowledge of the ionic conductivity σ_{ion}, we can directly calculate the ion concentration N_{ion}:

$$N_{ion} = \frac{\sigma_{ion}}{q \cdot \mu} \tag{8}$$

The calculated ion concentration N_{ion} at 293 K is 2.6×10^{16} cm^{-3} (Fig. 11c), which is higher but still close to previously reported values for polycrystalline $MAPbBr_3$ thin films [78]. As the temperature increases, the ion concentration rises to 3.1×10^{17} cm^{-3} at 383 K. This increase can be attributed to the thermally activated formation of mobile ionic defects, as discussed above.

The ion concentration extracted from impedance spectroscopy at 293 K is nearly two orders of magnitude lower than the trap density derived from TRPL measurements ($N_T = 1.6 \times 10^{18}$ cm^{-3}). However, a direct comparison between these two quantities is not straightforward, since they likely probe different subsets of defects, are sensitive to different regions of the film, and were obtained from differently processed samples. In particular, the ion concentration N_{ion} extracted from impedance spectroscopy was obtained from annealed films, for which thermal treatment may reduce certain defect populations. In contrast, TRPL measurements were taken on as-deposited films and are weighted toward the near-surface region, where the impact-driven PAD process may leave loosely compacted particles or defect-rich grain surfaces. Consequently, it is difficult to distinguish to what extent the observed discrepancy originates from annealing effects, different probing depths, or the different defect types involved. Nevertheless, the results indicate that aerosol-deposited $MAPbBr_3$ films still exhibit comparatively high defect densities despite their dense and void-free morphology. This highlights the importance of effective post-treatment strategies to further reduce defect densities and improve the optoelectronic performance of aerosol-deposited films.

Conclusions

In this work, we demonstrate the successful fabrication of pure $MAPbBr_3$ thin films at room temperature by powder aerosol deposition and provide a comprehensive analysis of their structural, optical, and electrical properties. The use of an ejector–separator unit and inertial separator proved essential for suppressing agglomerate-induced defects and enables the formation of dense, homogeneous films with good substrate adhesion. Structural analysis confirms that the phase purity and crystal structure is fully preserved during deposition, while impact-driven fragmentation leads to nanoscale crystallites (~ 90 nm) with low microstrain.

Optical characterization reveals that the bandgap of the aerosol-deposited films remains essentially unchanged compared to the precursor powder, indicating that the aerosol deposition process does not significantly alter the electronic structure. The structured photoluminescence emission is primarily attributed to self-absorption effects rather than additional defect-related recombination channels. Time-resolved measurements further indicate that the resulting films exhibit a relatively high density of traps, likely as a direct result of the deposition process.

Electrical characterization using temperature-dependent impedance spectroscopy revealed thermally activated ionic transport with activation energies of approximately 0.55–0.59 eV, which is consistent with the reported formation energy of bromide vacancies. Analyzing the dielectric loss tangent within the Trukhan framework quantitatively determined the ionic diffusion coefficient, mobility, and mobile ion concentration. The extracted diffusion coefficients (3.1×10^{-8} cm^2 s^{-1}), ionic mobility (1.2×10^{-6} cm^2 V^{-1} s^{-1}), and ion concentrations (2.6×10^{16} cm^{-3}) at 293 K are in good agreement with values reported in the literature for $MAPbBr_3$.

Overall, this study further establishes PAD as a solvent-free, scalable route for the fabrication of hybrid perovskite films while preserving intrinsic structural and optical properties.

Acknowledgements

We gratefully acknowledge the support and funding by the German Research Foundation (DFG) within CRC 1585 (project number 492723217) for sub-project B04. We acknowledge DESY (Hamburg, Germany), a member of the Helmholtz Association HGF, for the provision of experimental facilities. Portions of this research were carried out at PETRA III, and we would like to thank Dr. Volodymyr Baran for assistance in using beamline P02.1. Beamtime was allocated for proposal I-20240866. The authors also thank the Department of Metal and Alloys (Prof. Uwe Glatzel) for the possibility of conducting XRD measurements. We would like to thank Konstantin Müller for assistance in using the XRD device. We acknowledge the KeyLab Electron and Optical

Microscopy (Bayreuth, Germany), a KeyLab of the Bavarian Polymer Institute (BPI), for the provision of SEM (Zeiss LEO 1530). We would like to thank Ulrich Mansfeld and Martina Heider for assistance in using the SEM. We would like to thank Dr.-Ing. Jaroslaw Kita for performing the laser etching of the Al_2O_3 substrates with the C-IDEs structure. The author thanks Tobias Siegert, Maximilian Spies, Fatemeh Haddadi Barzoki, Philipp Ramming, Osama Alsheikha, Thomas Wöhrl, Lukas Hennerici, Jürgen Schneider, Mutlucan Sozak, Nils Donker, Monika Röthel, Simon Biberger, Nico Leupold, Michael König; Dillon Max Stevenson, Simon Freund, and Marius Kaiser for fruitful scientific discussions.

Author contributions

T. Xu was responsible for conceptualization, methodology, investigation, data curation, formal analysis, writing—original draft, and writing—reviewing and editing. M. Griesbach was involved in investigation (optical experiments), data curation, formal analysis, writing—original draft (optical sections), and writing—reviewing and editing. T. Scholz contributed to writing—reviewing and editing. D. Paulus took part in investigation (xrd experiments at desy), data curation, formal analysis, and writing—reviewing and editing. M. Hämmerle participated in validation, supervision, and writing—reviewing and editing. A. Köhler and R. Moos took care of validation, supervision, project funding acquisition, and writing—reviewing and editing.

Funding

Open Access funding enabled and organized by Projekt DEAL. Deutsche Forschungsgemeinschaft, 492723217, Ralf Moos and Anna Köhler.

Data availability

All datasets generated or analyzed during the current study are from the corresponding author on reasonable request.

Declarations

Conflict of interest The authors declare that they have no known competing financial interests or personal relationships that could have appeared to influence the work reported in this paper.

Supplementary Information The online version contains supplementary material available at https://doi.org/10.1007/s10853-026-13159-z.

References

[1] Green MA, Ho-Baillie A, Snaith HJ (2014) The emergence of perovskite solar cells. Nat Photonics 8:506–514. https://doi.org/10.1038/nphoton.2014.134

[2] Xing G, Mathews N, Sun S, Lim SS, Lam YM, Grätzel M, Mhaisalkar S, Sum TC (2013) Long-range balanced electron- and hole-transport lengths in organic-inorganic $CH_3NH_3PbI_3$. Science 342:344–347. https://doi.org/10.1126/science.1243167

[3] Kim G-W, Petrozza A (2020) Defect tolerance and intolerance in metal-halide perovskites. Adv Energy Mater 10:2001959. https://doi.org/10.1002/aenm.202001959

[4] Cho H, Jeong S-H, Park M-H, Kim Y-H, Wolf C, Lee C-L, Heo JH, Sadhanala A, Myoung N, Yoo S, Im SH, Friend RH, Lee T-W (2015) Overcoming the electroluminescence

efficiency limitations of perovskite light-emitting diodes. Science 350:1222–1225. https://doi.org/10.1126/science.aad1818

[5] Saidaminov MI, Adinolfi V, Comin R, Abdelhady AL, Peng W, Dursun I, Yuan M, Hoogland S, Sargent EH, Bakr OM (2015) Planar-integrated single-crystalline perovskite photodetectors. Nat Commun 6:8724. https://doi.org/10.1038/ncomms9724

[6] Mali SS, Shim CS, Hong CK (2015) Highly stable and efficient solid-state solar cells based on methylammonium lead bromide ($CH_3NH_3PbBr_3$) perovskite quantum dots. NPG Asia Mater 7:e208. https://doi.org/10.1038/am.2015.86

[7] Du Y, Feng Y, Liu W, Bai H, Yu Z, Zhao X, Liu K (2024) Wide-bandgap $MAPbBr_3$ perovskite solar cells using bifunctional-molecule additives achieving a high open-circuit voltage of 1.63 V. Surf Interfaces 51:104784. https://doi.org/10.1016/j.surfin.2024.104784

[8] McGovern L, Futscher MH, Muscarella LA, Ehrler B (2020) Understanding the stability of $MAPbBr_3$ versus MAPbI3: suppression of methylammonium migration and reduction of halide migration. J Phys Chem Lett 11:7127–7132. https://doi.org/10.1021/acs.jpclett.0c01822

[9] Stranks SD, Nayak PK, Zhang W, Stergiopoulos T, Snaith HJ (2015) Formation of thin films of organic-inorganic perovskites for high-efficiency solar cells. Angew Chem Int Ed 54:3240–3248. https://doi.org/10.1002/anie.201410214

[10] Ono LK, Leyden MR, Wang S, Qi Y (2016) Organometal halide perovskite thin films and solar cells by vapor deposition. J Mater Chem A 4:6693–6713. https://doi.org/10.1039/C5TA08963H

[11] Spies M, Biberger S, Eller F, Herzig EM, Köhler A (2025) Solvated PbI2 clusters preceding the crystallization of lead halide perovskites—a UV/VIS in situ study. Adv Electronic Mater 11:2500060. https://doi.org/10.1002/aelm.202500060

[12] Kim JH, Williams ST, Cho N, Chueh C-C, Jen AK-Y (2015) Enhanced environmental stability of planar heterojunction perovskite solar cells based on blade-coating. Adv Energy Mater 5:1401229. https://doi.org/10.1002/aenm.201401229

[13] Hwang K, Jung Y-S, Heo Y-J, Scholes FH, Watkins SE, Subbiah J, Jones DJ, Kim D-Y, Vak D (2015) Toward large-scale roll-to-roll production of fully printed perovskite solar cells. Adv Mater 27:1241–1247. https://doi.org/10.1002/adma.201404598

[14] Deng Y, Zheng X, Bai Y, Wang Q, Zhao J, Huang J (2018) Surfactant-controlled ink drying enables high-speed deposition of perovskite films for efficient photovoltaic modules. Nat Energy 3:560–566. https://doi.org/10.1038/s41560-018-0153-9

[15] Prat D, Wells A, Hayler J, Sneddon H, McElroy CR, Abou-Shehada S, Dunn PJ (2016) CHEM21 selection guide of classical and less classical solvents. Green Chem 18:288–296. https://doi.org/10.1039/C5GC01008J

[16] Akedo J, Park J-H, Kawakami Y (2018) Piezoelectric thick film fabricated with aerosol deposition and its application to piezoelectric devices. Jpn J Appl Phys 57:07LA02. https://doi.org/10.7567/JJAP.57.07LA02

[17] Ahn C-W, Choi J-J, Ryu J, Hahn B-D, Kim J-W, Yoon W-H, Choi J-H, Park D-S (2015) Microstructure and electrochemical properties of iron oxide film fabricated by aerosol deposition method for lithium ion battery. J Power Sources 275:336–340. https://doi.org/10.1016/j.jpowsour.2014.11.033

[18] Akedo J (2008) Room temperature impact consolidation (RTIC) of fine ceramic powder by aerosol deposition method and applications to microdevices. J Therm Spray Technol 17:181–198. https://doi.org/10.1007/s11666-008-9163-7

[19] Hanft D, Exner J, Schubert M, Stöcker T, Fuierer P, Moos R (2015) An overview of the aerosol deposition method: process fundamentals and new trends in materials applications. J Ceram Sci Technol 6:147–182. https://doi.org/10.4416/JCST2015-00018

[20] Panzer F, Hanft D, Gujar TP, Kahle F-J, Thelakkat M, Köhler A, Moos R (2016) Compact layers of hybrid halide perovskites fabricated via the aerosol deposition process—uncoupling material synthesis and layer formation. Materials 9:277. https://doi.org/10.3390/ma9040277

[21] Biberger S, Leupold N, Witt C, Greve C, Markus P, Ramming P, Lukas D, Schötz K, Kahle F-J, Zhu C, Papastavrou G, Köhler A, Herzig EM, Moos R, Panzer F (2023) First of their kind: solar cells with a dry-processed perovskite absorber layer via powder aerosol deposition and hot-pressing. Solar RRL 7:2300261. https://doi.org/10.1002/solr.202300261

[22] Cho M-Y, Kim S, Kim I-S, Kim E-S, Wang Z-J, Kim N-Y, Kim S-W, Oh J-M (2020) Perovskite-induced ultrasensitive and highly stable humidity sensor systems prepared by aerosol deposition at room temperature. Adv Funct Mater 30:1907449. https://doi.org/10.1002/adfm.201907449

[23] These A, Khansur NH, Almora O, Luer L, Matt GJ, Eckstein U, Barabash A, Osvet A, Webber KG, Brabec CJ (2021) Characterization of aerosol-deposited cesium lead tribromide perovskite films on interdigited ITO electrodes. Adv Electron Mater 7:2001165. https://doi.org/10.1002/aelm.202001165

[24] Dippel A-C, Liermann H-P, Delitz JT, Walter P, Schulte-Schrepping H, Seeck OH, Franz H (2015) Beamline P02.1 at PETRA III for high-resolution and high-energy powder

diffraction. J Synchrotron Radiat 22:675–687. https://doi.org/10.1107/S1600577515002222

[25] Pawley GS (1981) Unit-cell refinement from powder diffraction scans. J Appl Crystallogr 14:357–361. https://doi.org/10.1107/S0021889881009618

[26] Thompson P, Cox DE, Hastings JB (1987) Rietveld refinement of Debye–Scherrer synchrotron X-ray data from Al_2O_3. J Appl Crystallogr 20:79–83. https://doi.org/10.1107/S0021889887087090

[27] Balzar D, Ledbetter H (1993) Voigt-function modeling in Fourier analysis of size- and strain-broadened X-ray diffraction peaks. J Appl Crystallogr 26:97–103. https://doi.org/10.1107/S0021889892008987

[28] Makuła P, Pacia M, Macyk W (2018) How to correctly determine the band gap energy of modified semiconductor photocatalysts based on UV-Vis spectra. J Phys Chem Lett 9:6814–6817. https://doi.org/10.1021/acs.jpclett.8b02892

[29] Leupold N (2024) Aerosolbasierte Kaltabscheidung von Halogenidperowskiten vom Pulver zur Solarzelle. Doctoral thesis, University of Bayreuth, Shaker Verlag https://doi.org/10.15495/EPub_UBT_00007936

[30] Huang K-W, Li M-H, Chen Y-T, Wen Z-X, Lin C-F, Chen P (2024) Fast fabrication of μm-thick perovskite films by using a one-step doctor-blade coating method for direct X-ray detectors. J Mater Chem C 12:1533–1542. https://doi.org/10.1039/D3TC02736H

[31] Sakhatskyi K, Turedi B, Matt GJ, Wu E, Sakhatska A, Bartosh V, Lintangpradipto MN, Naphade R, Shorubalko I, Mohammed OF, Yakunin S, Bakr OM, Kovalenko MV (2023) Stable perovskite single-crystal X-ray imaging detectors with single-photon sensitivity. Nat Photonics 17:510–517. https://doi.org/10.1038/s41566-023-01207-y

[32] Wei H, Fang Y, Mulligan P, Chuirazzi M, Fang H-H, Wang C, Ecker BR, Gao Y, Loi MA, Cao L, Huang J (2016) Sensitive X-ray detectors made of methylammonium lead tribromide perovskite single crystals. Nat Photonics 10:333–339. https://doi.org/10.1038/nphoton.2016.41

[33] Qian W, Xu X, Wang J, Xu Y, Chen J, Ge Y, Chen J, Xiao S, Yang S (2021) An aerosol-liquid-solid process for the general synthesis of halide perovskite thick films for direct-conversion X-ray detectors. Matter 4:942–954. https://doi.org/10.1016/j.matt.2021.01.020

[34] Jaffe A, Lin Y, Beavers CM, Voss J, Mao WL, Karunadasa HI (2016) High-pressure single-crystal structures of 3D lead-halide hybrid perovskites and pressure effects on their electronic and optical properties. ACS Cent Sci 2:201–209. https://doi.org/10.1021/acscentsci.6b00055

[35] Wenger B, Nayak PK, Wen X, Kesava SV, Noel NK, Snaith HJ (2017) Consolidation of the optoelectronic properties of $CH_3NH_3PbBr_3$ perovskite single crystals. Nat Commun 8:590. https://doi.org/10.1038/s41467-017-00567-8

[36] Yamada T, Yamada Y, Nishimura H, Nakaike Y, Wakamiya A, Murata Y, Kanemitsu Y (2016) Fast free-carrier diffusion in CH3NH3PbBr$_3$ single crystals revealed by time-resolved one- and two-photon excitation photoluminescence spectroscopy. Adv Electronic Mater 2:1500290. https://doi.org/10.1002/aelm.201500290

[37] Schötz K, Askar AM, Peng W, Seeberger D, Gujar TP, Thelakkat M, Köhler A, Huettner S, Bakr OM, Shankar K, Panzer F (2020) Double peak emission in lead halide perovskites by self-absorption. J Mater Chem C 8:2289–2300. https://doi.org/10.1039/C9TC06251C

[38] Droseros N, Longo G, Brauer JC, Sessolo M, Bolink HJ, Banerji N (2018) Origin of the enhanced photoluminescence quantum yield in $MAPbBr_3$ perovskite with reduced crystal size. ACS Energy Lett 3:1458–1466. https://doi.org/10.1021/acsenergylett.8b00475

[39] Vila M, Bartolomé J, El Astal-Quirós A, Martínez-Pastor JP, Suarez I, de Andrés A, Coya C (2025) Morphology engineering of $MAPbBr_3$ thin films for enhanced lighting applications. APL Mater 13:071109. https://doi.org/10.1063/5.0263289

[40] Wu B, Nguyen HT, Ku Z, Han G, Giovanni D, Mathews N, Fan HJ, Sum TC (2016) Discerning the surface and bulk recombination kinetics of organic–inorganic halide perovskite single crystals. Adv Energy Mater 6:1600551. https://doi.org/10.1002/aenm.201600551

[41] Guo D, Bartesaghi D, Wei H, Hutter EM, Huang J, Savenije TJ (2017) Photoluminescence from radiative surface states and excitons in methylammonium lead bromide perovskites. J Phys Chem Lett 8:4258–4263. https://doi.org/10.1021/acs.jpclett.7b01642

[42] Steele JA, Puech P, Monserrat B, Wu B, Yang RX, Kirchartz T, Yuan H, Fleury G, Giovanni D, Fron E, Keshavarz M, Debroye E, Zhou G, Sum TC, Walsh A, Hofkens J, Roeffaers MBJ (2019) Role of electron–phonon coupling in the thermal evolution of bulk Rashba-like spin-split lead halide perovskites exhibiting dual-band photoluminescence. ACS Energy Lett 4:2205–2212. https://doi.org/10.1021/acsenergylett.9b01427

[43] Yuan Y, Yan G, Dreessen C, Rudolph T, Hülsbeck M, Klingebiel B, Ye J, Rau U, Kirchartz T (2024) Shallow defects and variable photoluminescence decay times up to 280 μs in triple-cation perovskites. Nat Mater 23:391–397. https://doi.org/10.1038/s41563-023-01771-2

[44] Jeong HJ, Bang S, Park DY, Jeon H, Namkoong G, Jeong MS (2020) Fabrication of pyramidal (111) $MAPbBr_3$ film with low surface defect density using homogeneous

quantum-dot seeds. Nanoscale 12:1366–1373. https://doi.org/10.1039/C9NR10070A

[45] Gao Z, Zheng Y, Zhao D, Yu J (2018) Spin-coated $CH3NH3PbBr_3$ film consisting of micron-scale single crystals assisted with a benzophenone crystallizing agent and its application in perovskite light-emitting diodes. Nanomaterials 8:787. https://doi.org/10.3390/nano8100787

[46] Baronnier J, Mahler B, Dujardin C, Houel J (2023) Low-temperature emission dynamics of methylammonium lead bromide hybrid perovskite thin films at the sub-micrometer scale. Nanomaterials 13:2376. https://doi.org/10.3390/nano13162376

[47] Arivazhagan V, Hang P, Parvathi MM, Tang Z, Khan A, Yang D, Yu X (2020) All-vacuum deposited and thermally stable perovskite solar cells with F4-TCNQ/CuPc hole transport layer. Nanotechnology 31:065401. https://doi.org/10.1088/1361-6528/ab4f2a

[48] Wolff CM, Caprioglio P, Stolterfoht M, Neher D (2019) Nonradiative recombination in perovskite solar cells: the role of interfaces. Adv Mater 31:e1902762. https://doi.org/10.1002/adma.201902762

[49] Witt C, Schötz K, Kuhn M, Leupold N, Biberger S, Ramming P, Kahle F-J, Köhler A, Moos R, Herzig EM, Panzer F (2023) Orientation and grain size in $MAPbI_3$ thin films: influence on phase transition, disorder, and defects. J Phys Chem C 127:10563–10573. https://doi.org/10.1021/acs.jpcc.2c08968

[50] Zhao Q, Zhang B, Hui W, Su Z, Wang H, Zhang Q, Gao K, Zhang X, Li B-H, Gao X, Wang X, de Wolf S, Wang K, Pang S (2024) Oxygen vacancy mediation in SnO_2 electron transport layers enables efficient, stable, and scalable perovskite solar cells. J Am Chem Soc 146:19108–19117. https://doi.org/10.1021/jacs.4c03783

[51] Lee JH, Lee S, Kim T, Ahn H, Jang GY, Kim KH, Cho YJ, Zhang K, Park J-S, Park JH (2023) Interfacial α-$FAPbI_3$ phase stabilization by reducing oxygen vacancies in SnO_{2-x}. Joule 7:380–397. https://doi.org/10.1016/j.joule.2022.12.006

[52] Luchkin SY, Akbulatov AF, Frolova LA, Griffin MP, Dolocan A, Gearba R, Vanden Bout DA, Troshin PA, Stevenson KJ (2017) Reversible and irreversible electric field-induced morphological and interfacial transformations of hybrid lead iodide perovskites. ACS Appl Mater Interfaces 9:33478–33483. https://doi.org/10.1021/acsami.7b01960

[53] Cho H, Kim JS, Kim Y-H, Lee T-W (2018) Influence of A-site cation on the thermal stability of metal halide perovskite polycrystalline films. J Inf Disp 19:53–60. https://doi.org/10.1080/15980316.2018.1424652

[54] Da S-J, Liu W-W, Li C-X, Lei Y-X, Ran F (2025) Regulation of interface Schottky barrier and photoelectric properties in carbon-based HTL-free perovskite solar cells. Small 21:e2408923. https://doi.org/10.1002/smll.202408923

[55] Irvine JTS, Sinclair DC, West AR (1990) Electroceramics: characterization by impedance spectroscopy. Adv Mater 2:132–138. https://doi.org/10.1002/adma.19900020304

[56] Bouchet R, Knauth P, Laugier J-M (2006) Theoretical analysis of the impedance spectra of electroceramics. Part 2: isotropic grain boundaries. J Electroceram 16:229–238. https://doi.org/10.1007/s10832-006-8278-9

[57] Kidner NJ, Homrighaus ZJ, Ingram BJ, Mason TO, Garboczi EJ (2005) Impedance/dielectric spectroscopy of electroceramics. Part 2: grain shape effects and local properties of polycrystalline ceramics. J Electroceram 14:293–301. https://doi.org/10.1007/s10832-005-0968-1

[58] Meggiolaro D, Mosconi E, de Angelis F (2019) Formation of surface defects dominates ion migration in lead-halide perovskites. ACS Energy Lett 4:779–785. https://doi.org/10.1021/acsenergylett.9b00247

[59] Xing J, Wang Q, Dong Q, Yuan Y, Fang Y, Huang J (2016) Ultrafast ion migration in hybrid perovskite polycrystalline thin films under light and suppression in single crystals. Phys Chem Chem Phys 18:30484–30490. https://doi.org/10.1039/C6CP06496E

[60] Walsh A, Stranks SD (2018) Taking control of ion transport in halide perovskite solar cells. ACS Energy Lett 3:1983–1990. https://doi.org/10.1021/acsenergylett.8b00764

[61] Senocrate A, Maier J (2019) Solid-state ionics of hybrid halide perovskites. J Am Chem Soc 141:8382–8396. https://doi.org/10.1021/jacs.8b13594

[62] Thiesbrummel J, Milić JV, Deibel C, Garnett EC, Tao S, Kirchartz T, Guerrero A, Cameron P, Tress W, Islam MS, Ehrler B (2026) Ion migration in perovskite solar cells. Nat Rev Chem 10:179–195. https://doi.org/10.1038/s41570-025-00790-8

[63] Mannodi-Kanakkithodi A, Park J-S, Martinson ABF, Chan MKY (2020) Defect energetics in pseudo-cubic mixed halide lead perovskites from first principles. J Phys Chem C 124:16729–16738. https://doi.org/10.1021/acs.jpcc.0c02486

[64] Reichert S, An Q, Woo Y-W, Walsh A, Vaynzof Y, Deibel C (2020) Probing the ionic defect landscape in halide perovskite solar cells. Nat Commun 11:6098. https://doi.org/10.1038/s41467-020-19769-8

[65] Ullah S, Andrio A, Marí-Guaita J, Ullah H, Méndez-Blas A, Del Castillo Vázquez RM, Mari B, Compañ V (2024) An intrinsic electrical conductivity study of perovskite powders $MAPbX_3$ (X = I, Br, Cl) to investigate its effect on their photovoltaic performance. Phys Chem Chem Phys 26:6736–6751. https://doi.org/10.1039/D3CP05686D

[66] Wang Y, Sun CN, Fan F, Sangoro JR, Berman MB, Greenbaum SG, Zavadil KR, Sokolov AP (2013) Examination of methods to determine free-ion diffusivity and number density from analysis of electrode polarization. Phys Rev E 87:042308. https://doi.org/10.1103/PhysRevE.87.042308

[67] Munar A, Andrio A, Iserte R, Compañ V (2011) Ionic conductivity and diffusion coefficients of lithium salt polymer electrolytes measured with dielectric spectroscopy. J Non-Cryst Solids 357:3064–3069. https://doi.org/10.1016/j.jnoncrysol.2011.04.012

[68] Singh R, Singh PK, Singh V, Bhattacharya B (2019) Quantitative analysis of ion transport mechanism in biopolymer electrolyte. Opt Laser Technol 113:303–309. https://doi.org/10.1016/j.optlastec.2018.12.036

[69] Sørensen TS, Compañ V (1995) Complex permittivity of a conducting, dielectric layer containing arbitrary binary Nernst–Planck electrolytes with applications to polymer films and cellulose acetate membranes. J Chem Soc, Faraday Trans 91:4235–4250. https://doi.org/10.1039/FT9959104235

[70] Boersma A, van Turnhout J (1998) Dielectric study on size effects in polymer laminates and blends. J Polym Sci Part B Polym Phys 36:2835–2848

[71] Nuevo D, Cuesta M, Porcar R, Andrio A, Garcia-Verdugo E, Compañ V (2023) Novel electrolytes based on mixtures of dimethyl sulfoxide task-specific zwitterionic ionic liquid and lithium salts: synthesis and conductivity studies. Chem Phys 575:112043. https://doi.org/10.1016/j.chemphys.2023.112043

[72] Alvarez AO, Lédée F, García-Batlle M, López-Varo P, Gros-Daillon E, Guillén JM, Verilhac J-M, Lemercier T, Zaccaro J, Marsal LF, Garcia-Belmonte G, Almora O (2023) Ionic field screening in $MAPbBr_3$ crystals revealed from remnant sensitivity in X-ray detection. ACS Phys Chem Au 3:386–393. https://doi.org/10.1021/acsphyschemau.3c00002

[73] García-Batlle M, Baussens O, Amari S, Zaccaro J, Gros-Daillon E, Verilhac J-M, Guerrero A, Garcia-Belmonte G (2020) Moving ions vary electronic conductivity in lead bromide perovskite single crystals through dynamic doping. Adv Electronic Mater 6:2000485. https://doi.org/10.1002/aelm.202000485

[74] García-Batlle M, Deumel S, Huerdler JE, Tedde SF, Almora O, Garcia-Belmonte G (2022) Effective ion mobility and long-term dark current of metal halide perovskites with different crystallinities and compositions. Adv Photonics Res 3:2200136. https://doi.org/10.1002/adpr.202200136

[75] García-Batlle M, Deumel S, Huerdler JE, Tedde SF, Guerrero A, Almora O, Garcia-Belmonte G (2021) Mobile ion-driven modulation of electronic conductivity explains long-timescale electrical response in lead iodide perovskite thick pellets. ACS Appl Mater Interfaces 13:35617–35624. https://doi.org/10.1021/acsami.1c06046

[76] García-Batlle M, Mayén Guillén J, Chapran M, Baussens O, Zaccaro J, Verilhac J-M, Gros-Daillon E, Guerrero A, Almora O, Garcia-Belmonte G (2022) Coupling between ion drift and kinetics of electronic current transients in $MAPbBr_3$ single crystals. ACS Energy Lett 7:946–951. https://doi.org/10.1021/acsenergylett.1c02578

[77] Peng W, Aranda C, Bakr OM, Garcia-Belmonte G, Bisquert J, Guerrero A (2018) Quantification of ionic diffusion in lead halide perovskite single crystals. ACS Energy Lett 3:1477–1481. https://doi.org/10.1021/acsenergylett.8b00641

[78] McGovern L, Koschany I, Grimaldi G, Muscarella LA, Ehrler B (2021) Grain size influences activation energy and migration pathways in $MAPbBr_3$ perovskite solar cells. J Phys Chem Lett 12:2423–2428. https://doi.org/10.1021/acs.jpclett.1c00205